ScienceDirect

Results in Chemistry

Volume 6, December 2023, 101083

Magneto-optical properties of Fe-doped bismuth oxide nanorods for photocatalytic and antimicrobial applications

V.A. Mane [a], D.V. Dake [a], N.D. Raskar [a], R.B. Sonpir [a], E. Stathatos [b], B.N. Dole [a]

Show more

https://doi.org/10.1016/j.rechem.2023.101083

Get rights and content

Abstract

Pure and Fe-doped Bi_2O_3 nanorods were synthesized using a hydrothermal method and characterized by XRD, FTIR, Raman, FE-SEM, BET, UV–VIS, VSM, and PL. The impact of Fe doping on Bi_2O_3 causes variation in properties. The 0.5% Fe-doped sample exhibited high surface area ($21.732 m^2/g$) and defects, resulting in exceptional photocatalytic efficiency (93.37%) for Methylene Blue dye degradation under visible light. In addition, their magnetic properties were also investigated, along with observing improved antimicrobial activity. The 0.5% Fe-doped Bi_2O_3 exhibited a notable 20mm diameter zone of inhibition against bacteria and 23mm against fungi, highlighting. This study highlights the versatile potential of Fe-doped Bi_2O_3 nanorods in photocatalysis and antimicrobial applications.

Graphical abstract

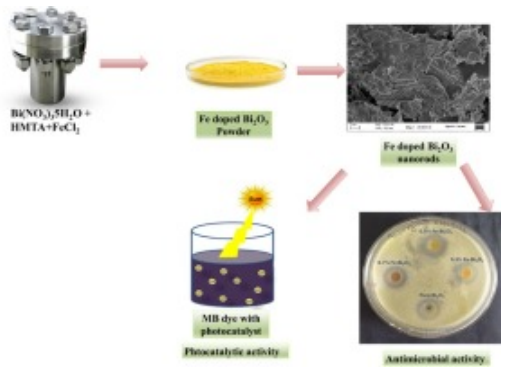

Download : Download high-res image (108KB)

Download : Download full-size image

Previous Next

Keywords

Fe-doped Bi_2O_3; Hydrothermal treatment; Photocatalytic effect; Antimicrobial

Introduction

In environmental protection, the quest for stable photocatalysts with enhanced antimicrobial activity that exhibit specific electrical and optical characteristics, with strong photoactivity mainly in the visible, to be harmless and cost-effective using ecological methods of fabrication is of high interest nowadays [1]. Numerous types of research are going on the photocatalytic activity and antibacterial activity for various pollutants and bacteria utilizing various semiconductor materials, including TiO_2 [2], ZnO [3], [4], CuO [5], SnO_2 [6], Bi_2O_3 [7], [8], Fe_2O_3 [9], GO-based composites [10]. Because of its cost-effective, harmless, and oppose to photo corrosion nature, titanium oxide has been the most widely used for photocatalytic application. TiO_2 has a large band gap (3.2 eV), which lowers its photo response in the visible part of the spectrum and restricts the range of its viable uses [11]. Therefore, it was thought that semiconductor photocatalysts operated by visible light might be useful for removing contaminants from the environment [12]. Gold (Au) [13] and silver (Ag) [14] based nanomaterials have been employed in treatments of microbial infections and have shown great results. However, due to its diverse and multifunctional features, narrow band gap (2.1–2.8 eV) nano-structural Bi_2O_3 has emerged as a promising photocatalyst among oxide semiconductors that may be employed for antimicrobial activity. Bismuth oxide's efficient electron conductivity emerges from its essential polarizability, which is caused by the Bi $6s^2$ lone electron pairs [15]. Bi_2O_3 is a semiconductor of the p-type with six different phases of crystalline structure [16], which are α-Bi_2O_3(Monoclinic) [17], β-Bi_2O_3(tetragonal) [18], γ-Bi_2O_3(Body-centered cubic) [19] and δ-Bi_2O_3(Face

cantered cubic) [20], ε-Bi2O3(orthorhombic) [21], and φ-Bi2O3 (triclinic) [22] respectively. Among them, the α-Bi_2O_3 monoclinic phase is stable at low-temperature and the δ-Bi_2O_3 cubic phase is stable at high-temperature, while the other phases are metastable at high-temperature.

One of the best applications of Bi_2O_3 is photocatalytic activity and antimicrobial activity. Photocatalytic activity occurs on the surface of Bi_2O_3 [23]. Bismuth oxide (Bi_2O_3) has antibacterial capabilities due to its crystal structure (cubic and monoclinic phases), which influences its contact with microorganisms [24]. When it comes into contact with fluids, it produces reactive oxygen species (ROS), which are harmful to bacterial components. Bi_2O_3 nanoparticles cause leaks and ion imbalances in cell membranes, obstruct enzymatic activities, and perturb cell surfaces, compromising integrity and nutrient absorption [25]. Bismuth ions released from Bi_2O_3 upon fluid contact add to bacterial cell damage. These effects make Bi_2O_3 a potential antibacterial agent. But Because of the rapid recombination of photo-generated electron-hole pairs, the photocatalytic activity and antimicrobial activity of pure bismuth oxide is rather low [26]. Inspired by this issue, it is critical to take steps to prevent electron and hole recombination. To solve this problem and to enhance the properties of photocatalytic and antibacterial activity of Bi_2O_3, it could be doped with some metal ions like Fe, Cr, Zn, Ag, Cu, Sn, etc. Doping of Fe ions act as electron traps, limiting recombination of photo-generated electron-hole pairs, improving charge separation capacity and utilization of these charges for photocatalytic processes, resulting in increased activity [27]. Recently, doping of Fe has shown enhancement in the photocatalytic activity of semiconductors made of TiO_2 and C_3N_4 for the production of ammonia [28]. Fe doping can enhance antimicrobial activity due to its ability to generate reactive oxygen species (ROS) via photocatalysis. These ROS, like hydroxyl radicals, attack microbial cell walls and components, promoting microbial degradation [29].

Pure and Fe-doped Bi_2O_3 were synthesized using a hydrothermal method and thoroughly characterized through XRD, FTIR, Raman, FESEM, EDAX, UV-DRS, VSM, BET, and PL analysis. The impact of Fe doping on Bi_2O_3's phase transition, crystalline size, surface area, defects, and magnetization was studied. Fe doping influenced these properties, with varying effects at different concentrations. Regarding applications, Fe doping exhibited a remarkable influence on the photocatalytic and antimicrobial properties of Bi_2O_3. The incorporation of Fe ions led to enhanced photocatalytic activity, attributed to improved charge separation and surface reactivity. Additionally, Fe-doped Bi_2O_3 demonstrated an amplified antimicrobial effect, ascribed to the generation of reactive oxygen species. This dual enhancement in photocatalysis and antimicrobial activity underscores the innovation and multifunctionality of Fe-doped Bi_2O_3, paving the way for novel applications in environmental and healthcare domains.

Experimental details

Synthesis of pure and Fe doped bismuth oxide

The chemicals employed were all analytical pure-grade chemicals provided by Fisher Scientific

Company, and neither of them required further decontamination. Pure and Fe-doped Bi_2O_3 nanorods with various concentrations(0, 0.3, 0.5, and 0.7%) were made via hydrothermal synthesis. For the synthesis of pure Bi_2O_3 nanoparticles, 0.2 M Bismuth Nitrate Pentahydrate (98%) and 1 M Hexamethyltetramine (99%) were separately dissolved in 25 mL of DI water. HMTA solution was incorporated while stirring continuously to the Bismuth Nitrate pentahydrate solution. To keep the pH at 12, ammonia was added drop by drop, and the solution was continuously stirred for an hour. The solution was placed into the Teflon-lined stainless steel autoclave. In a muffle furnace, the autoclave was tightly sealed and the temperature was maintained at 150 °C for 12 h. Then the system was cooled at room temperature. The prepared samples were filtered and washed with DI water and ethanol. Finally, all the samples were dried at room temperature. HMTA, bismuth nitrate pentahydrate, and ferrous chloride hydrated (98%) were used in the production of Fe-doped Bi_2O_3 at concentrations of 0.3%, 0.5%, and 0.7%.

Photocatalytic experiment

The dye degradation experiment of the pure Bi_2O_3 and Fe-doped Bi_2O_3 nanorod was evaluated by quantifying the amount of azo dye that was decorated during exposure to natural sunlight. During the photocatalysis, 100 mL of dye solution of Methylene blue (MB) containing 20 mg L^{-1} of the species' concentration (C_0) was added to the 0.2 g photocatalyst powder. Before being exposed to natural sunlight for irradiation, the final MB solution was continuously stirred for 20 min in a darkroom.

In Aurangabad, Maharashtra, India, during the summer, samples of produced dyes were exposed to solar light from 11 a.m. to 2 p.m. for the photocatalytic experiment. 19.85°N and 75.35°E are the latitude and longitude, respectively. The average daily solar energy output for the summer was determined to be about 6.80 kWh/m2/day. The photocatalyst were separated using centrifugation at 500 rpm for 5 mins before UV–Vis measurements. Approximately 2 mL of the sample was injected, and the absorbance spectra of the degraded solution were recorded to monitor the observed absorption peak, which was analyzed to assess the extent of degradation of each species. This was done at 30-min intervals of illumination. After 20 min of stirring, MB dye was subjected to natural sunshine irradiation between the hours of 11 a.m. and 2 p.m. During this time, photocatalyst powder dropped to the bottom of the beaker and was collected for use in subsequent processes, such as the degradation of recycled materials.

Antibacterial experiment

The antibacterial activity of the synthesized pure and Fe-doped Bi_2O_3 was tested using the well diffusion technique with the gram-positive bacterium Bacillus. The sterilized Petri plates were filled with the prepared Nutrient agar and allowed to solidify. It was swabbed with 24-hour developing bacterial cultures (E. coli). A cork borer was used to create the four wells (10 mm in diameter). Dimethyl sulphoxide was used to dissolve pure and Fe-doped Bi_2O_3 nanorods, which were then placed into the wells. The plates were then incubated for 24 h at 37°Celsius. The inhibition diameter

was measured after incubation.

Antifungal experiment

The antifungal activity of the Pure and Fe-doped Bi_2O_3 nanorods was evaluated using a well diffusion technique. To perform this test, fungi named, Aspergillus *flavus were* selected. Then, 30 mL potato dextrose agar and agar agar powder were poured into the sterile petri dish and allowed to solidify. Pure and Fe-doped Bi_2O_3 nanorods were dissolved in Dimethyl sulphoxide and loaded in the wells. The plates were incubated for 24–48 hr for fungi stains. The antifungal activity of the samples was determined by measuring the inhibition zone (mm).

Materials characterizations

The characterization of Pure and Fe-doped Bi2O3 samples involved a range of techniques. To determine structural parameters, X-ray diffraction patterns were obtained using a D-8 Advanced diffractometer (Bruker AXS, Germany) with monochromatic CuKα radiation and a scintillator detector. Surface morphology and elemental composition were studied using Field Emission Scanning Electron Microscope (FE-SEM) and energy-dispersive X-ray analysis (EDAX) on a ZEISS Gemini FE-SEM. Optical properties, including absorption and fluorescence spectra, were examined using an Avantes UV–Vis spectrometer with a Photoluminescence study. Chemical bonding was explored via Fourier transform infrared spectroscopy (FT-IR) on a Bruker, Germany, model: Vertex 70 spectrometer, in the wavelength range of 500–4000 cm^{-1}. Raman spectroscopy (Perkin Elmer) was employed to investigate vibrational and phonon modes. Specific surface area, pore radius, and pore volume were determined using Quanta chrome ASiQwin 1994–2017 BET Autosorb iQ instrument system, utilizing the dynamic Brunner–Emmet–Teller (BET) method with N2 gas adsorption at 77.35 K. Magnetic properties were measured using VSM (VSM 7403) at room temperature and magnetic field ±10 KOe. These techniques collectively provided comprehensive insights into the properties of the samples.

Results and discussion

XRD

Fig. 2 depicts the X-ray diffraction pattern of pure Bi_2O_3 and Fe-doped Bi_2O_3 nanorods. According to the XRD pattern, pure Bi_2O_3 nanorods have a monoclinic structure with space group P21/c [30]. 23.84°, 25.69°, 27.33°, 30.19°, 33.03, 37.54°, 46.29°, 52.32° are the observed 2θ peaks, and which are consistent with α-Bi_2O_3 (0 2 0), (0 0 2), (−1 2 0), (0 1 2), (2 0 0), (1 1 2), (0 4 1), (0 3 3), lattice planes. The obtained XRD result is consistent with the previously reported publications (JCPDS card no: 00–014-0699) [31]. The lattice parameters of the synthesized pristine α-Bi_2O_3 are found to be a=5.8500 Å, b=8.1660 Å, and c=7.5100 Å using the formulae below [31].

$$\frac{1}{d^2} = \frac{1}{sin^2\beta}\left(\frac{h^2}{a^2} + \frac{k^2 sin^2\beta}{b^2} + \frac{l^2}{c^2} - \frac{2hlcos\beta}{ac}\right.$$

After doping of Fe, a monoclinic phase has been changed to cubic Fe doped δ-Bi_2O_3. In Fig. 1. (b) (c) (d) at 23.84°, 27.48°, 30.19°, 33.03, 42.22°, 46.99°, 52.25°, 56.90° are the observed 2θ peaks and so on are consistent with cubic (0.3%, 0.5%, 0.7%) Fe-Bi_2O_3 (2 2 0), (3 1 0), (2 2 2), (3 2 1), (3 3 2), (5 2 1), (0 3 5), (6 2 0), lattice planes. The occurrence of Fe-doped Bi_2O_3 may be categorized as a surface (interface) effect. As the concentration of Fe increased, the cubic phase took predominance [32]. As shown by the results in Fig. 1, this pattern also appears at higher temperatures. The strength of the peaks rises as the concentration of Fe rises. This cubic phase's lattice parameter is determined to be a=9.4808 using the formula below:

$$\frac{1}{d^2} = (h^2+k^2+l^2)\frac{1}{c^2}$$

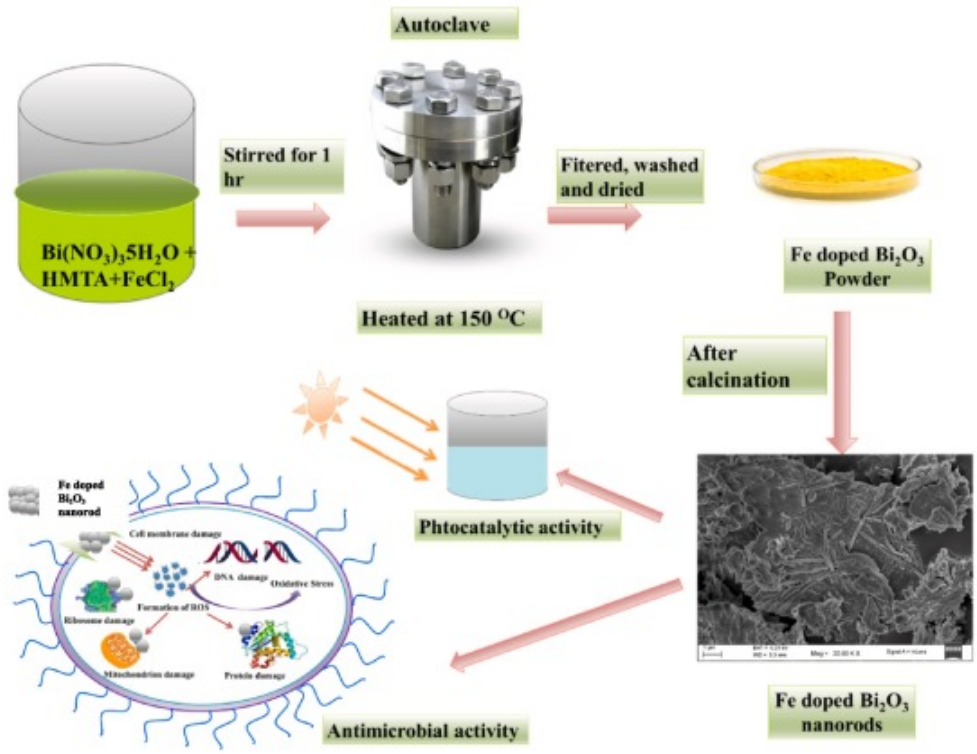

Download : Download high-res image (361KB)

Download : Download full-size image

Fig. 1. Schematic diagram of the synthesis of pure and Fe-doped Bi_2O_3 nanorods.

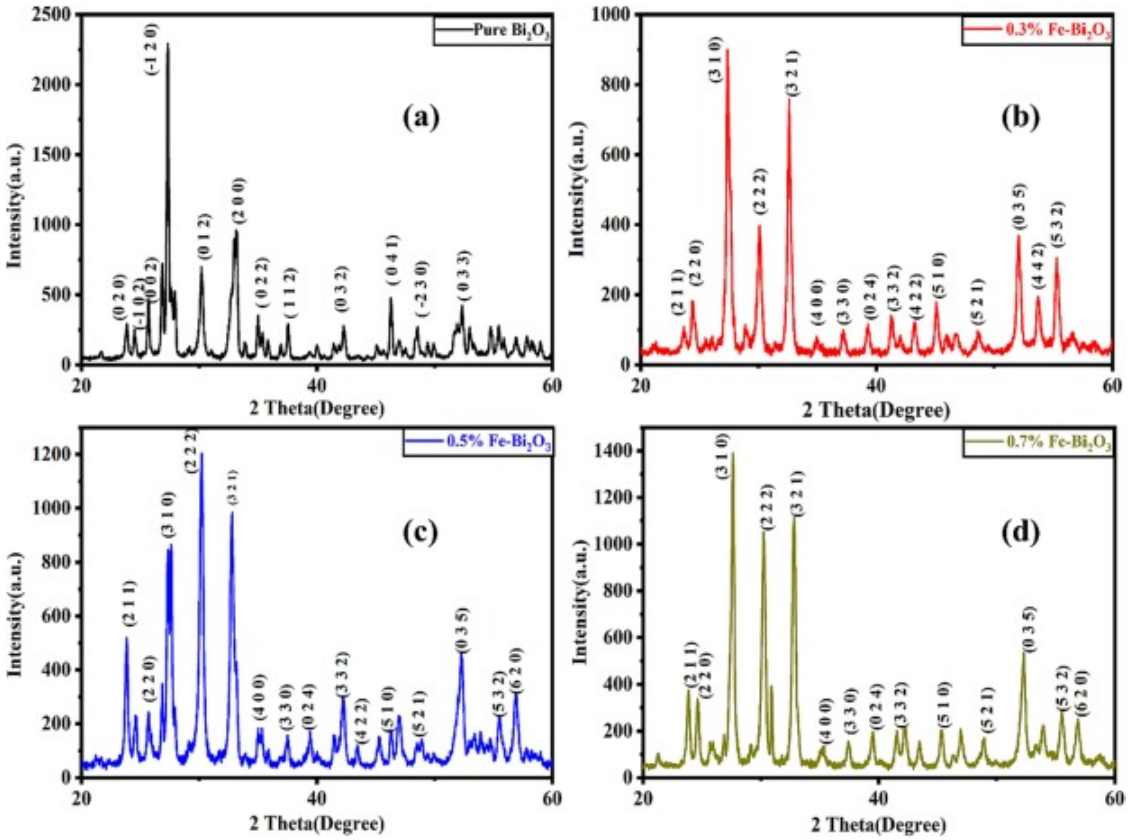

Download : Download high-res image (432KB)

Download : Download full-size image

Fig. 2. XRD graphs of Pure Bi_2O_3 and 0.3%, 0.5% and 0.7% Fe doped Bi_2O_3.

The crystallite size was calculated by the Debye-Sherrer formula and the lattice parameters including dislocation density (δ), microstrain (ε), and stacking fault (SF) were also calculated and summarized in Table 1 [1]. From the following equations, the crystallite characteristics of all samples, dislocation density, microstrain, and existent stacking faults were analyzed.

$$\text{Dislocation density } (\delta) = \frac{1}{D^2}$$

$$\varepsilon) = \frac{\beta cos\theta}{4}$$

$$\text{Stacking fault } (S.F) = [\frac{2\pi^2}{45(3tan\theta)^{\frac{1}{2}}}]\beta$$

Table 1. Calculated crystallographic parameters of pure and Fe-doped Bi_2O_3 samples.

Sample	Volume $(A)^3$	Crystallite Size (nm)	Dislocation Density (lines/ $m^{2)}$	Microstrain (e)	Stacking Fault (SF)
Pure Bi_2O_3	331.67	37.00	0.00117	0.00109457	0.002184

Sample	Volume $(A)^3$	Crystallite Size (nm)	Dislocation Density (lines/ $m^{2)}$	Microstrain (e)	Stacking Fault (SF)
0.3% Fe-Bi_2O_3	839.01	25.91	0.00152	0.00134097	0.002573
0.5% Fe-Bi_2O_3	852.20	25.44	0.00176	0.00141822	0.002714
0.7% Fe-Bi_2O_3	757.43	27.45	0.00136	0.00126035	0.002385

When the concentration of Fe changes from 0%, 0.3%, 0.5%, and 0.7%, the crystallite size reduces from 37 to 25 nm. Additionally, it shows that Bi_2O_3 with greater Fe doping has a larger unit cell capacity. Fe doping disrupts Bi_2O_3's atomic arrangement and stability, inducing lattice distortions and defects due to differences in size and charge between Fe and Bi ions [33]. This shift favors a cubic phase due to distinct ionic radii [26]. Doping a small amount (0.5%) of Fe to Bi_2O_3 disrupts its crystal structure due to differences in ion sizes. This creates defects, hindering crystal growth and causing the size to decrease. Higher(0.7%) Fe concentration promotes nucleation, aiding new domain formation, slightly increasing Bi_2O_3 crystalline size. More grain boundaries develop as the grain size decreases, and the number of dislocations rises as one-dimensional defects occur, which is a result of the doping of Fe [34]. We observe that when crystallite size decreases, microstrain and dislocation density enhances. The presence of defects in the material is indicated by the dislocation density, microstrain, and stacking faults. These defects in Fe-doped Bi_2O_3 enhance photocatalytic activity by slowing the recombination rate of photoexcited charge carriers [35].

FTIR analysis

The chemical composition of prepared Pristine and Fe-doped Bi_2O_3 powders was examined by FTIR spectroscopy in the range of 500–4000 cm^{-1} and data are given in Fig. 3. Bi-O vibrations may have been responsible for the strong peak at 1386 cm^{-1} [36] which is well-matched with the published literature [30], [37]. With an increase in the doping percentage, a significant rise in peak intensity was seen. When Bi ions were doped with Fe ions in the Bi-O lattice, the density of the defect state around the Bi ions changed, which was the reason for the increase in peak intensity [38]. Doping with Fe ions reduces grain size. For NPs, it is a frequent occurrence that tiny variations in the environment cause a shift in the distinctive vibrational frequencies of functional groups. The increase in vibrational frequency results from the reduction in grain size [39]. Fig. 3 shows that the two significant vibrational mode frequencies, ν_1 and ν_2, are present in the spectra and fall around the range of 575––560 cm^{-1} and 540–520 cm^{-1}, respectively. The stretching at the interstitial tetrahedral (A) and octahedral (B) sublattices is attributed to these two vibrational mode frequencies (ν_1 and ν_2), respectively [40]. Wavenumber and stretching of the material are depicted in Table 2.

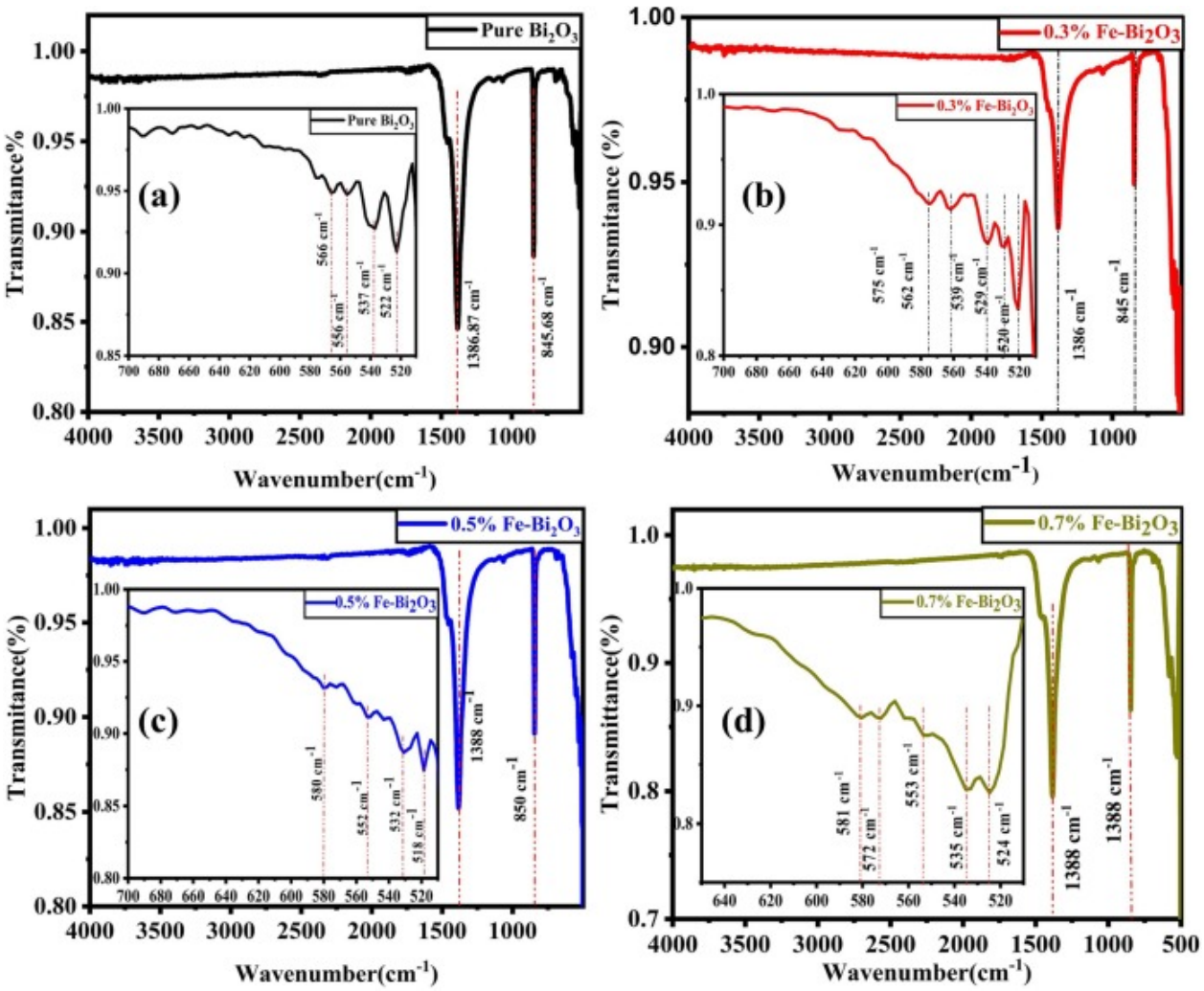

Download : Download high-res image (683KB)

Download : Download full-size image

Fig. 3. FT-IR spectra of pure and (0.3%, 0.5%, and 0.7%) Fe-doped Bi_2O_3 samples.

Table 2. Wavenumber and stretching for the synthesized pure and Fe-doped Bi_2O_3.

Sr. No.	Wavenumber	Stretching
1	1388	Bi-O
2	850	Bi-O
3	580	Fe-O
4	552	Fe-O
5	518	Fe-O

Raman spectroscopy

Raman spectroscopy aids in the analysis and characterization of material composition, crystalline structure, and defects present in a variety of materials, including polymers, semiconductors, ceramics, and nanomaterials [41]. Raman spectra of pure and Fe-doped Bi_2O_3 were observed in the range 0–1200cm^{-1} in Fig. 4. According to group theory, irreducible representation for optical modes with well-existing $15A_g+15B_g$ for monoclinic Bi_2O_3 is given by [42]:

$$\Gamma = 15A_g + 15B_g + 14A_u + 1B_u$$

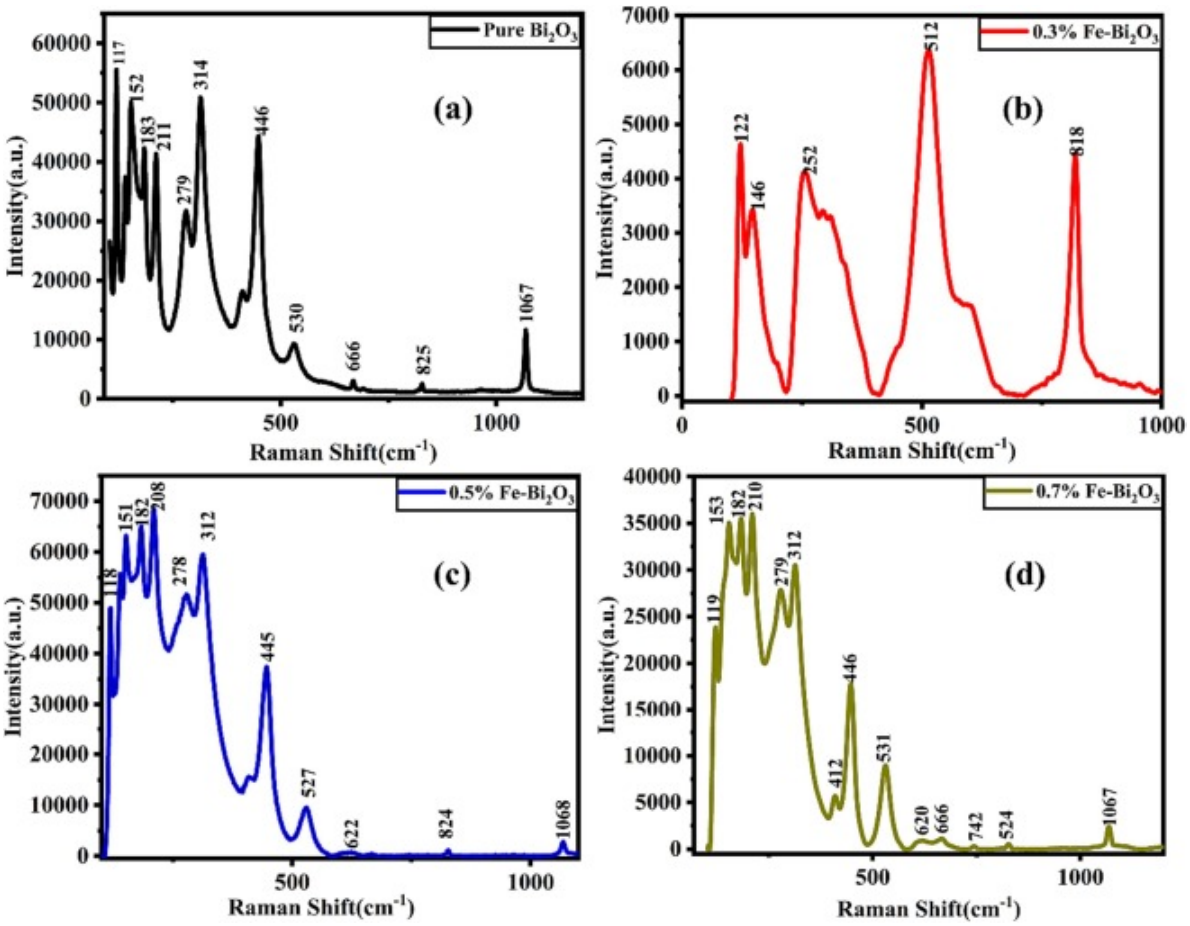

Download : Download high-res image (433KB)

Download : Download full-size image

Fig. 4. Raman spectra of Pure Bi_2O_3 and (0.3%, 0.5%, and 0.7%) Fe doped Bi_2O_3.

Four first-order Raman modes are active: the non-degenerated A_{1g}, $B1_{g.}$ and B_{2g} modes and the doubly degenerated E_g mode. A_{2g} and B_{1u} are silent modes. One A_{2u} and two Eu modes are acoustic and have transverse (TO) and longitudinal optical (LO) vibrations [43]. Energy position (cm^{-1}), Overtones, and obtained from RAMAN spectroscopy for the Pure Bi_2O_3, Fe doped Bi_2O_3 samples were depicted in Table 3. The movements of the Bi cations from configurations are responsible for the Raman bands in the spectral area between 50 and 500cm^{-1}, while the Bi-O-Bi and Bi-O vibrations produce the bands in the region between 200 and 550cm^{-1} [37]. Raman spectra of Bi_2O_3 samples are often described by considering three distinct regions: below 120cm^{-1}, between 120 and

150cm^{-1}, and above 150cm^{-1} [42], [44]. The Bi-O stretching, or the displacement of O concerning Bi is what causes the vibrational modes at 152 and 183cm^{-1}. The vibration of the same oxygen atom in the Bi_2O_3 structure is responsible for the peak at 210cm^{-1}. The symmetric stretching vibrations of the Bi-O atoms represented by (A_g, B_g) were held accountable for the band at 314cm^{-1} [45], [46]. In addition to new bands appearing, certain peaks also move to the higher wavenumber side, showing an increase in force constants following Fe doping. As can be observed from the plots, the doping action of Fe in Bi_2O_3 has caused the peaks to move to higher frequencies [47]. Additionally, a band due to oxygen vacancies (as defects) was noticed at around 530cm $^{-1}$. Raman spectra shows one Raman active phonon of T_{2g} at 622cm^{-1} [48]. A careful examination of the Raman spectra of the Fe doped-Bi_2O_3 shows weak bands 666,724, 826, and 1064cm^{-1} that could be associated with the rearrangement of the anionic sub-lattice, i.e. oxygen ions and vacancies [49].

Table 3. Energy position (cm^{-1}), Overtones, and obtained from RAMAN spectroscopy for the Pure Bi_2O_3, 0.3% Fe-Bi_2O_3, 0.3% Fe-Bi_2O_3, 0.3% Fe-Bi_2O_3 samples.

Pure Bi_2O_3 (cm^{-1})	**0.3% Fe-Bi_2O_3 (cm^{-1})**	**0.5% Fe-Bi_2O_3 (cm^{-1})**	**0.7% Fe-Bi_2O_3 (cm^{-1})**	**Overtones and combinations**
117	122	118	119	A_g
152	146	151	153	B_g
183		182	182	A_{1g}
211		208	210	B_u
279	252	278	279	B_g
314		312	312	(A_g)
446		445	446	B_g
530	512	527	531	A_g
		622	620	T_{2g}
666				
			724	
1067		1068	1067	

Microscopy analysis (FE-SEM)

FE-SEM was used to examine the surface topography of the produced Bi_2O_3. Fig. 5. Shows high-resolution images of pure and Fe-doped Bi_2O_3 which has a thick and agglomerated nanorod-like structure. It's intriguing to note that a small number of the nanorods are joined at one of their bases, which may be the result of the nanorods growing in high density and have a random orientation.

The surface roughness and the microscopic particles grow denser and narrower after Fe doping; hence, the agglomeration of the nanorods with adjacent ones may be related to the greater relative surface-to-volume ratio, which causes an increase in forces of attraction among the nanoparticles [50]. The smaller nanorods that are connected to the larger nanorods in the micrographs may also be observed in addition to the high aspect ratio nanorods. The nanorods have smooth, pristine surfaces all along their length [30].

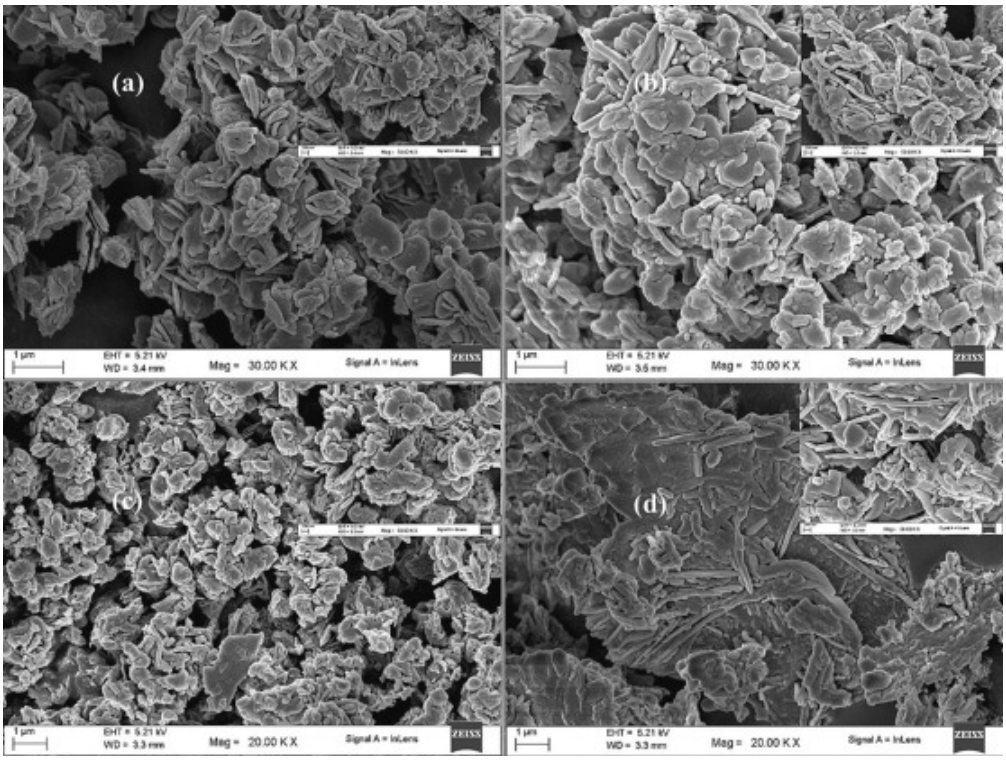

Download : Download high-res image (493KB)

Download : Download full-size image

Fig. 5. SEM micrographs of a) Pure Bi_2O_3 and b)0.3%, c)0.5%, and d) 0.7% Fe doped Bi_2O_3 with various concentrations.

EDS analysis

The fundamental composition of synthesized materials is examined using energy-dispersive X-ray analysis (EDAX), which is also used to confirm the proper incorporation of dopants and the production of Bi_2O_3 nanoparticles. Fig. 6 displays the EDAX signals of pure Bi_2O_3 and Fe-doped Bi_2O_3 at various concentrations. Sharp indications of Bi and oxygen were discovered for pure Bi_2O_3 nanoparticles, indicating the growth of the particles as illustrated in Fig. 6 a. For the Fe-doped sample, Fe signals were additionally discovered to the Bi and oxygen signals, demonstrating that Fe was effectively incorporated into the Bi_2O_3 in Fig. 6 b, c, and d.

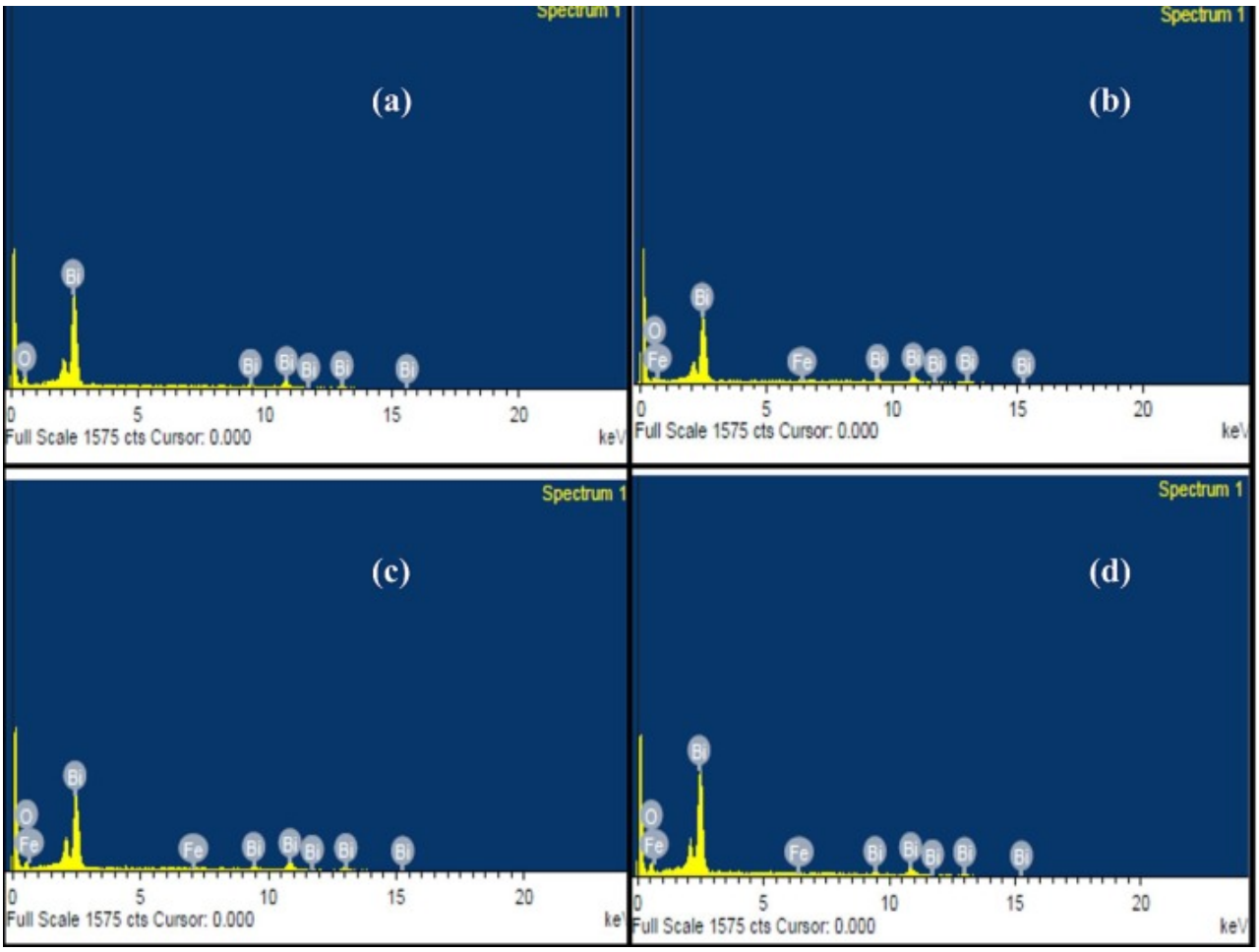

Download : Download high-res image (147KB)

Download : Download full-size image

Fig. 6. EDS graphs of Pure Bi_2O_3 and (0.3, 0.5, and 0.7%) Fe doped Bi_2O_3.

The elemental composition of pure and Fe-doped Bi_2O_3 nanorods was depicted in Table 4. The obtained Fe-doped Bi_2O_3 compositions are pure and free of contaminants, which is an essential point to consider.

Table 4. Elemental composition of pure and Fe-doped Bi_2O_3 nanorods.

Samples	**Bi(%)**	**O(%)**	**Fe(%)**	**Total**
Pure Bi_2O_3	23.55	76.45	–	100
0.3% Fe-Bi_2O_3	24.98	75.77	0.25	100
0.5% Fe-Bi_2O_3	25.86	73.67	0.47	100
0.7% Fe-Bi_2O_3	23.14	76.18	0.68	100

UV–Vis diffuse reflectance spectra

Using DRS at room temperature, the optical reflectance of each sample of pure Bi_2O_3 and Fe-doped Bi_2O_3 was examined. The results are presented in Fig. 7. The reflectance spectra for pure Bi_2O_3 are assigned to 430nm. The reflectance spectra have been allocated a wavelength between 420 and 500nm. Fe particle doping affects the band gap tuning in a way that causes the band gap to narrow as it approaches the UV region. Recognizing the quantization effect and the interaction of doping with Fe-Bi_2O_3 is made simpler due to this absorption spectrum. The electron transition from the valence band to the conduction band, which corresponds to the reduction in the gap between the bands after doping, can be seen in the reflectance spectrum of the doped catalyst at about 430nm.

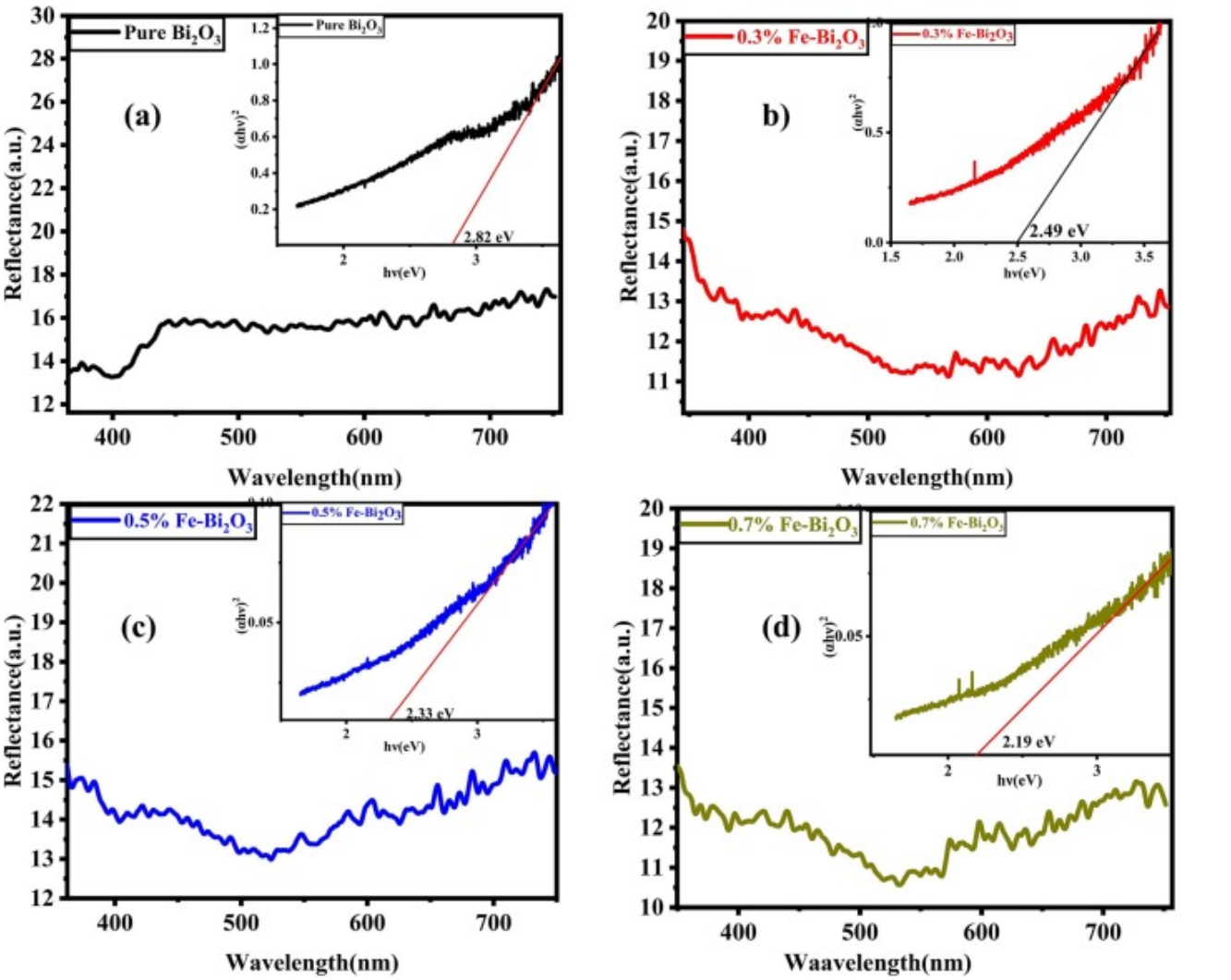

Download : Download high-res image (517KB)

Download : Download full-size image

Fig. 7. UV–VIS spectra of Pure Bi_2O_3 and 0.3%, 0.5% and 0.7% Fe doped Bi_2O_3.

The most well-known "Tauc plot" $[(\alpha h\upsilon)^2$ v/s $(h\upsilon)]$ was developed with the assistance of UV–Vis reflectance spectral data to determine the optical bandgap energy (Eg) values of the produced

samples. Additionally, based on the DRS results, the band gap energies of the samples as prepared were determined using the formula (1)

$$\alpha h\upsilon = A(h\upsilon - Eg)^{n/2} \quad (1)$$

where α, h, υ, Eg, and A are the absorption coefficient, Plank constant, light frequency, band gap energy, and a constant, respectively. Among these, n is governed by the semiconductor's optical transition type. As a result, the Eg was estimated to be between 2.82 and 2.19, as shown in Table 2 below, using a plot of (αhυ)1/2 vs energy (hυ). Synthesized samples of pure Bi_2O_3 and Fe-doped Bi_2O_3 with varying Fe concentrations are shown in Table 5. The table shows that the band gap reduces as the concentration of Fe rises. The significant interaction of the band boundary of the electron transition between the molecules of bismuth, oxygen, and Fe is demonstrated by the redshift caused by the addition of Fe dopant [51]. The significant red shift in the band gap seen may thus be explained by the sp-d exchange interaction between valance band electrons and confined d electrons of Fe in Bi_2O_3. Positive and negative corrections to valence and conduction bands were caused by sp-d exchange interactions; as a result, band-gap narrowing occurred in systems with sp-d exchange interactions [52]. The formation of electrons and holes will be considerably simpler when excitation due to the effect of photon energy from UV light irradiation takes place because the energy required for electrons to travel from the valence band to the conduction band is decreasing [53]. The photocatalytic activity can be increased by increasing the creation of electrons and holes [54].

Table 5. Synthesized Samples and their observed band gaps.

Samples	**Band Gap (Eg)**
Pure Bi_2O_3	2.82eV
0.3% Fe-Bi_2O_3	2.49eV
0.5% Fe-Bi_2O_3	2.33eV
0.7% Fe-Bi_2O_3	2.19eV

Magnetic properties

The magnetic behavior of Fe-doped Bi_2O_3 material depends on the alignment and interaction of magnetic moments within the crystal lattice. At ambient temperature, VSM was used to analyze the magnetic behavior of the powder made from synthesized Fe-doped bismuth oxide nanoparticles. Fig. 8 displays the field-dependent magnetization curves of pure Bi_2O_3 and Fe-doped Bi_2O_3 at different concentrations. Table 6 summarises the measured values of saturation magnetization, coercivity, retentivity, remanence ratio, and magnetron number for both pure and Fe-doped Bi_2O_3. From the table we can see that, the magnetization saturation value of the Bi_2O_3 and (0.3, 0.5, and 0.7%) Fe doped Bi_2O_3 core was measured to be 0.15353, 0.20429, 0.85175, and 0.5765 emu/gm. 0.5%

Fe-doped Bi_2O_3 shows the highest magnetization as compared to other samples. The coercivity of the prepared samples was found to be 45.310, 39.426, 28.395, and 34.761 Oe.

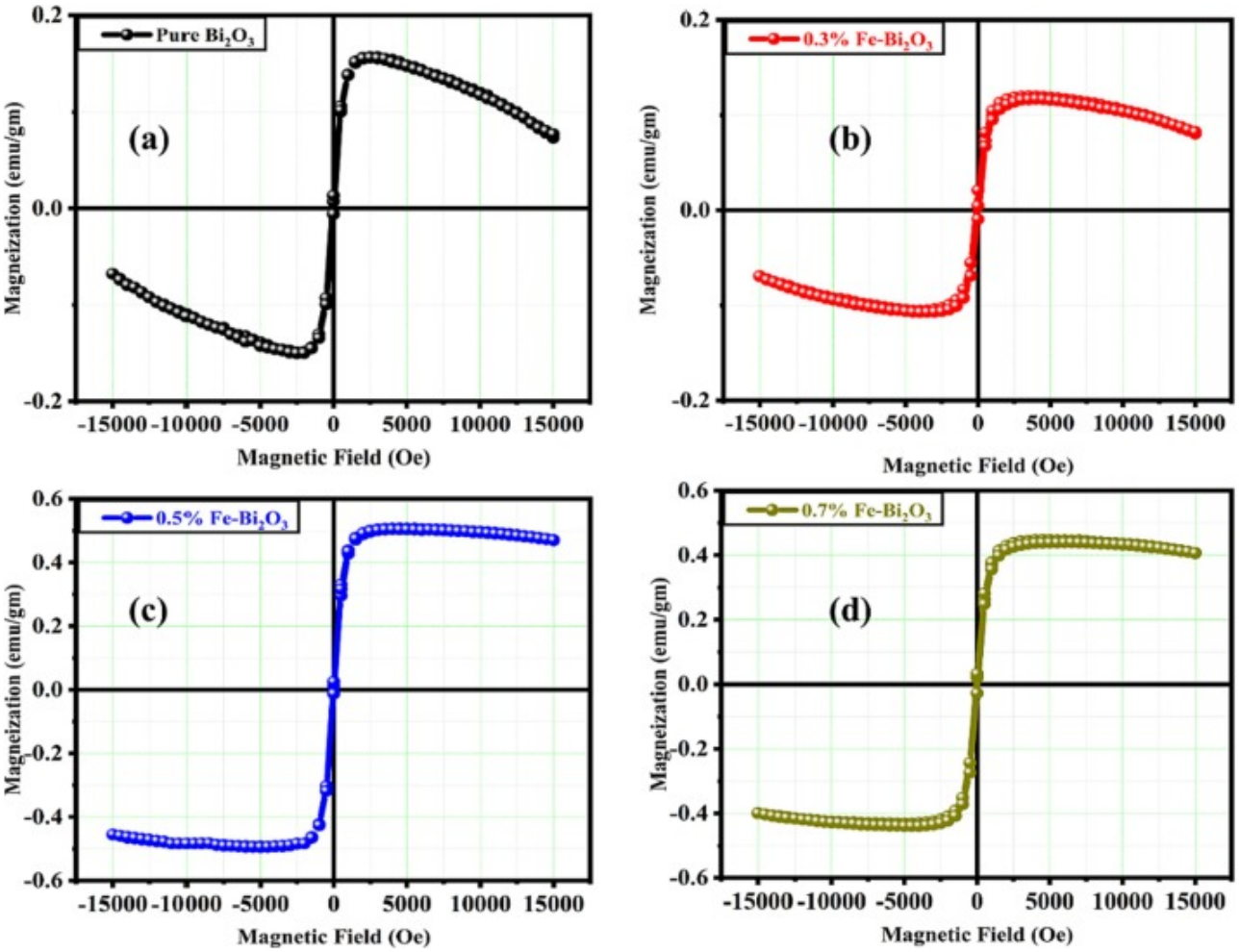

Download : Download high-res image (525KB)

Download : Download full-size image

Fig. 8. VSM Spectra of pure Bi_2O_3 and 3%, 5% and 7% Fe doped Bi_2O_3.

Table 6. Calculated Magnetic properties of pure and Fe-doped Bi_2O_3.

Samples	Coercivity Oe	Magnetization (M_s) emu/gm	Retentivity (M_r) emu/gm	Remanence ratio/ Retentivity ratio	Magnetron Number (nB)
Pure Bi_2O_3	45.310	0.15353	0.009665	0.062953	0.543416
0.3 % Fe-Bi_2O_3	39.426	0.20429	0.027319	0.133727	0.715697
0.5 % Fe-Bi_2O_3	28.395	0.85175	0.031677	0.03719	0.093641

Samples	Coercivity Oe	Magnetization (M_s) emu/gm	Retentivity (M_r) emu/gm	Remanence ratio/ Retentivity ratio	Magnetron Number (nB)
0.7% Fe-Bi_2O_3	34.761	0.5765	0.039301	0.068172	0.135803

After Fe was doped in the Bi_2O_3 shell, the saturation magnetization increased while the coercivity decreased. At 0.5% Fe doping in Bi_2O_3, magnetization is optimized due to cooperative interactions between dopants and the lattice. Exceeding this optimal level (0.7%) disrupts crystal structure, forming non-magnetic phases, and decreases magnetism. Higher concentrations introduce defects, altering the crystal arrangement and reducing magnetization. Two processes in nanoparticles may contribute to a decrease in coercivity: (a) changing from a single-domain to a multi-domain state, and (b) a decrease in surface anisotropy with particle size [55]. All the investigated materials' M–H graphs at room temperature (Fig. 9) had superparamagnetic characteristics as shown by minimal coercivity and remanence magnetization. As a result of the increased density of the bulk and lattice strain in the current situation, magnetization values have increased. Additionally, the Pure Bi_2O_3 and Fe-doped Bi_2O_3 samples had multi-domain structures, as shown by the remanence ratio (M_r/M_S) value is too low in comparison to 0.5 [56]. According to the aforementioned discussion, an increase in magnetization is primarily related to an increase in oxygen vacancies in addition to the presence of magnetic Fe ions within the Bi_2O_3 lattice. These findings are in good agreement with PL results, and they explain how superparamagnetic behavior develops in Fe-doped Bi_2O_3 nanostructures [57]. According to this evidence, the material could show enhanced photocatalytic and antimicrobial gestures.

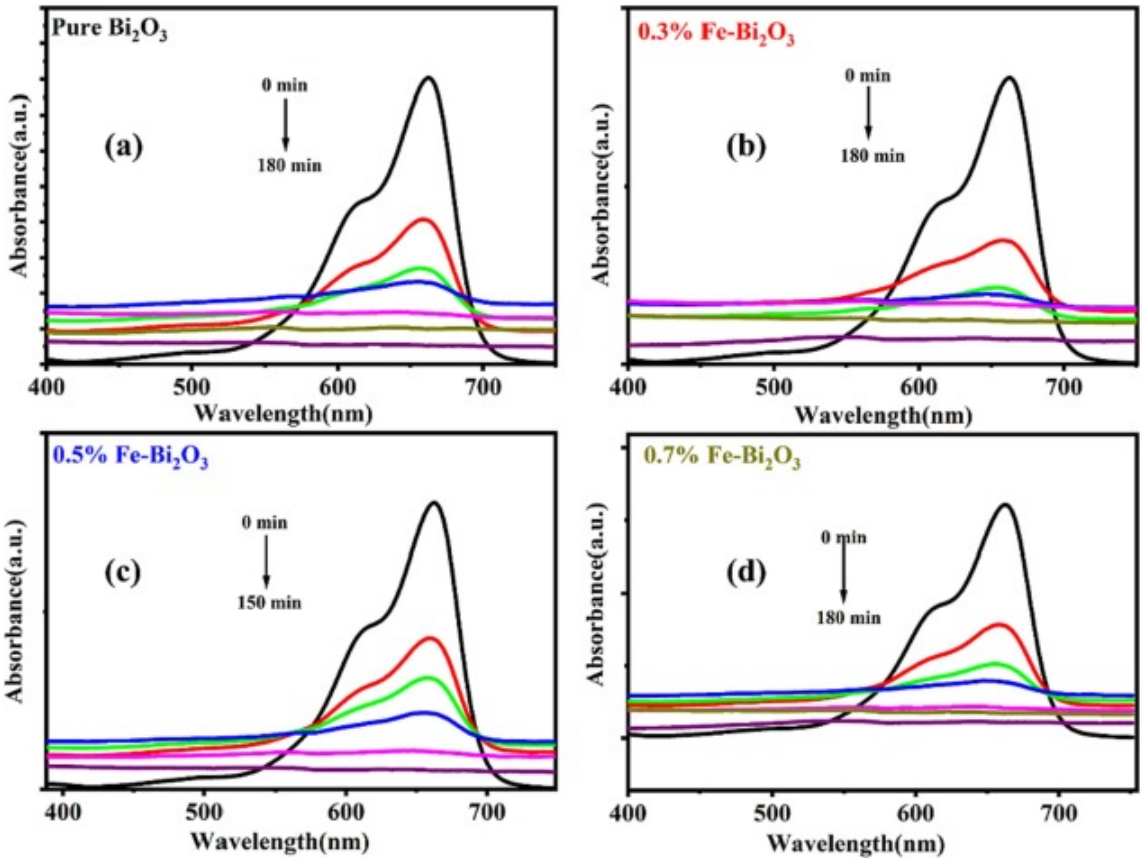

Download : Download high-res image (401KB)

Download : Download full-size image

Fig. 9. Photodegradation of Methylene Blue dye by **(a)** Pure Bi_2O_3, (**b)** 0.3% Fe-Bi_2O_3, 0.5% Fe-$Bi_2O_3$and (**c)** 0.7% Fe-Bi_2O_3. (For interpretation of the references to colour in this figure legend, the reader is referred to the web version of this article.)

Photocatalytic activity

It would be reasonable to assume that reducing crystal size, expanding surface area, and red-shifting absorption edges might all improve photocatalytic activity in photocatalysts. The photocatalytic effectiveness of each powder as it was fabricated was examined and depicted in Fig. 9. One of the most challenging naturally degradable dyes is methylene blue. The photocatalytic activities of Pure and Fe-doped Bi_2O_3 nanoparticles were interfered with to investigate the effects of transition metal doping on the degradation rate. The MB dye's photodegradation in aqueous solution when exposed to sunlight was used. The maximal photodegradation was estimated using the formula below to determine the photodegradation efficiency in (%):

$$Photodegradation Efficiency(\%) = \left(\frac{C_0 - C_{100}}{C_0}\right) X100$$

The findings of kinetic investigations on pure and Fe-doped Bi_2O_3 samples are depicted in Fig. 10 a and b. Our samples correspond to the relationship shown below for the photodegradation of

methylene blue, which is a pseudo-first-order kinetics connection.

$$log\,\frac{C_0}{C_t} = kt$$

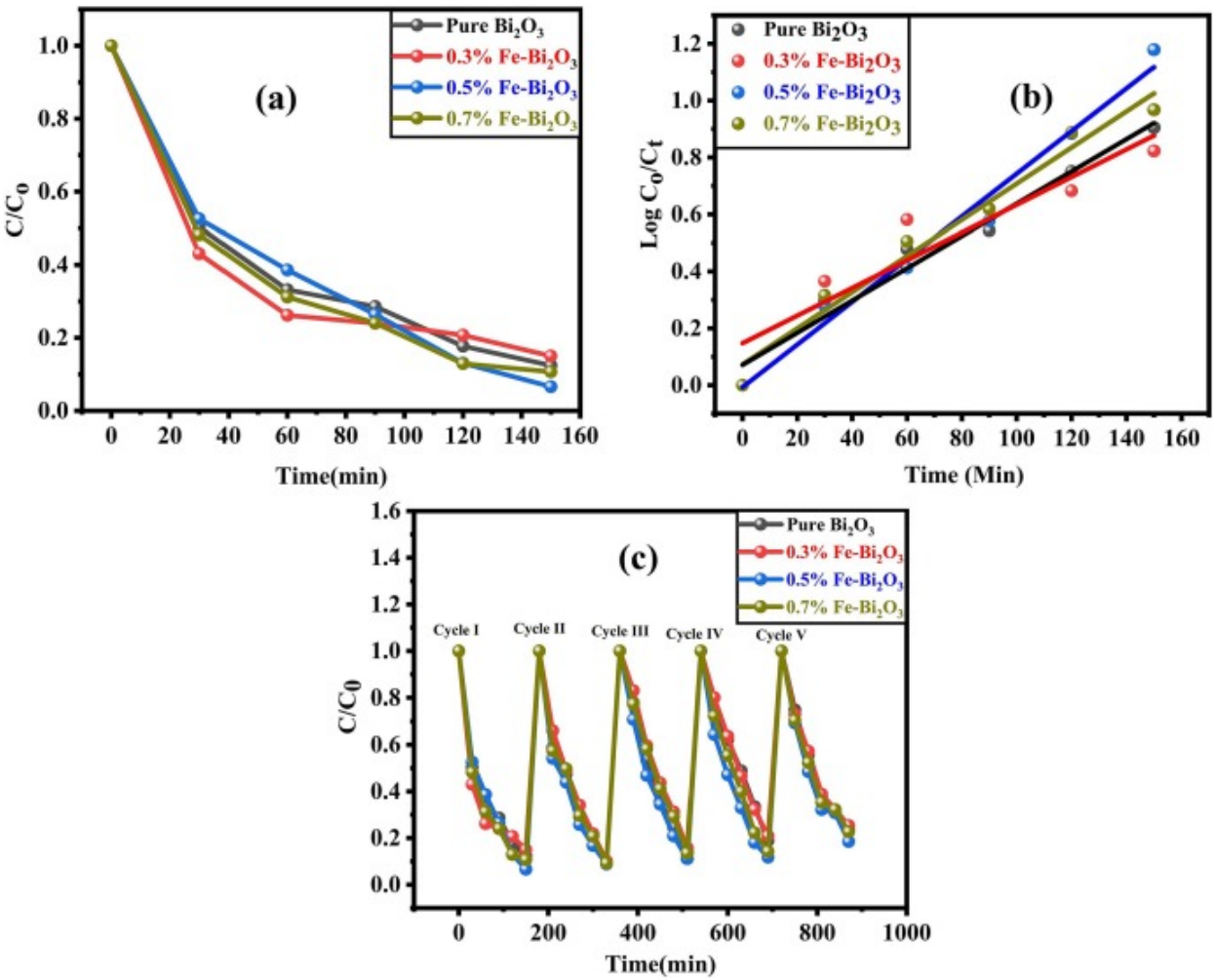

Download : Download high-res image (464KB)

Download : Download full-size image

Fig. 10. a) Plot of time versus C/C_0 and b) plot of time versus log (C_0/C_t) and c) Variation of the relative concentration of MB dye solution under visible light irradiation in the presence of pure Bi_2O_3 and 0.3%, 0.5%and 0.7% Fe-doped Bi_2O_3 nanorods over 5 cycles.

Table 5 included information on the photodegradation effectiveness and pseudo-first-order rate constant (k) of unsubstituted and Fe-substituted Bi_2O_3 samples. Pure Bi_2O_3 and samples with 0.3%, 0.5%, and 0.7% Fe substituted Bi_2O_3 had photodegradation efficiency that was 87.50%, 84.96%, 93.37%, and 89.21%, respectively. Variations in recyclability were observed, and this was specifically confirmed. According to Fig. 10 (c), recycling was shown in the Pure Bi_2O_3 and the 0.3%, 0.5%, and 0.7% Fe substituted Bi_2O_3 samples. The photocatalytic effectiveness decreased after the five cycles were finished, but the chemical stability was still good.

Table 7. gives information about the comparison of previously published and present research work of Fe doped photocatalyst.

Table 7. Comparison of previously published and present research work of Fe doped photocatalyst.

Sr. No	Sample	Synthesis Method	Source	Dye	Efficiency	Reference
1.	Fe doped TiO_2	Wet impregnation method	UV light irradiation	MB	19% in 150min	[58]
2.	Fe doped ZnO	Co-precipitation method	UV light irradiation	MB	58% in 150min	[59]
3.	Fe doped TiO_2	Impregnation method	LED solar simulator	Rh.B	85% in 3.5 hr	[60]
4.	Fe doped CdO	Hydrothermal	Visible source	MB	58.8% for 80min	[61]
5.	Fe doped Bi_2O_3	Hydrothermal	Sunlight	MB	93.37% in 150min	Present Work

Photodegradation efficiency and Pseudo-first-order rate constant (k) of pure and Fe-substituted Bi_2O_3 samples are incorporated in Table 8. Due to the synergistic interaction between Fe and Bi_2O_3, the photocatalytic activity of Fe-doped Bi_2O_3 is greater than that of pure Bi_2O_3. The material that is doped with 0.5% Fe has the highest degrading efficiency (93.37%), and the rate constant k=0.0075 at 150min. According to the results, adding Fe to Bi_2O_3 up to a concentration limit of 0.5% would boost photocatalytic activity, but adding more above 0.5% will reduce it, as indicated in the table below. These findings align with earlier studies [33]. The BET analysis findings show 0.5% Fe-doped Bi_2O_3 has a large surface area and a large specific surface area can boost photocatalytic activity. The fluorescence intensity of the 0.5% Fe-doped Bi_2O_3 nanorod is greater than all samples from the blue and green emission range. An increase in the intensity of the green emission might mean that the 0.5% Fe-doped Bi_2O_3 nanorods have more defects or more surface oxygen vacancies, both of which are essential for photocatalytic activity. So the incorporation of Fe ions altered the crystal structure, introducing lattice distortions and defects. This modifies the Bi_2O_3's electronic properties, enhancing charge carrier mobility and separation. Consequently, Fe doping has modified the average crystalline size and surface area. These alterations collectively enhance the material's photocatalytic efficiency by facilitating better light absorption, extended surface interactions, and improved charge transfer kinetics.

Table 8. Photodegradation efficiency and Pseudo-first-order rate constant (k) of pure and Fe-substituted Bi_2O_3 samples.

Sample	Cycle I		Cycle II		Cycle III		Cycle IV	
	Photocatalytic Efficiency	Pseudo Rate Constant	Photocatalytic Efficiency	Pseudo Rate Constant	Photocatalytic Efficiency	Pseudo Rate Constant	Photocatalytic Efficiency	Pseu Rate Cons
Pure	87.5	0.0057	90.57	0.0063	85.81	0.0056	81.05	0.004

Sample	Cycle I		Cycle II		Cycle III		Cycle IV	
	Photocatalytic Efficiency	Pseudo Rate Constant	Photocatalytic Efficiency	Pseudo Rate Constant	Photocatalytic Efficiency	Pseudo Rate Constant	Photocatalytic Efficiency	Pseu Rate Cons
Bi_2O_3								
0.3% Fe-Bi_2O_3	84.96	0.0049	89.90	0.0063	84.29	0.0052	79.08	0.004
0.5% Fe-Bi_2O_3	93.37	0.0075	91.08	0.0067	88.80	0.0062	88.20	0.006
0.7% Fe-Bi_2O_3	89.21	0.0063	90.73	0.0064	86.46	0.0056	85.72	0.005

Porosity analysis

It is generally recognized that the specific surface area of the photocatalyst has a greater impact on the degradation effectiveness of photocatalytic activity and antimicrobial activity. Using the BET approach, the surface area of pure and Fe-doped Bi_2O_3 nanorods was determined. The pore size distribution graphs of pure and Fe-doped Bi_2O_3 nanorods, as well as the nitrogen adsorption–desorption isotherms, are presented in Fig. 11. According to the IUPAC system of classification and as shown in Fig. 11, the isotherms of pure Bi_2O_3 and the 0.3, 0.5, and 0.7% Fe-Bi_2O_3 nanorods are typical type-IV N_2 adsorption–desorption isotherms with H_1 hysteresis, indicate the presence of mesoporous structure. The particle's surface area predictions were computed using the N_2 adsorption–desorption isotherms. For both pure and Fe-doped Bi_2O_3 nanorods, the BJH technique was used to determine the BET surface area, pore volume, and pore diameter. These results are shown in Table 8. The surface for pure Bi_2O_3 was discovered to be 7.722 m^2/g. The surface area was determined to be 3.765, 21.732, and 11.704 m^2/g for various Fe-doped concentrations like 0.3, 0.5, and 0.7%, respectively. As seen in Table 8, it can be seen that the surface area rises as the Fe dopant concentration increases. However, the 0.5% Fe-doped Bi_2O_3 has the largest surface area (21.732 m^2/g) due to the sample's smallest crystallite size. Due to the surface of the lowest energy plane, a 0.5% Fe-doped Bi_2O_3 sample has a greater surface area than other samples. The surface area of the 0.5% Fe-doped Bi_2O_3 sample is higher than that of other samples because this smallest energy surface may adsorb more N_2 gas than another sample. Because of Fe doping in the Bi_2O_3 lattice, surface area increases can be allocated to the appearance of new pores. The ultimately enhanced surface area of Fe-doped Bi_2O_3 should be connected to the phase shift and reduced crystalline size, which are brought on by Fe doping, as compared to pure Bi_2O_3 [26].

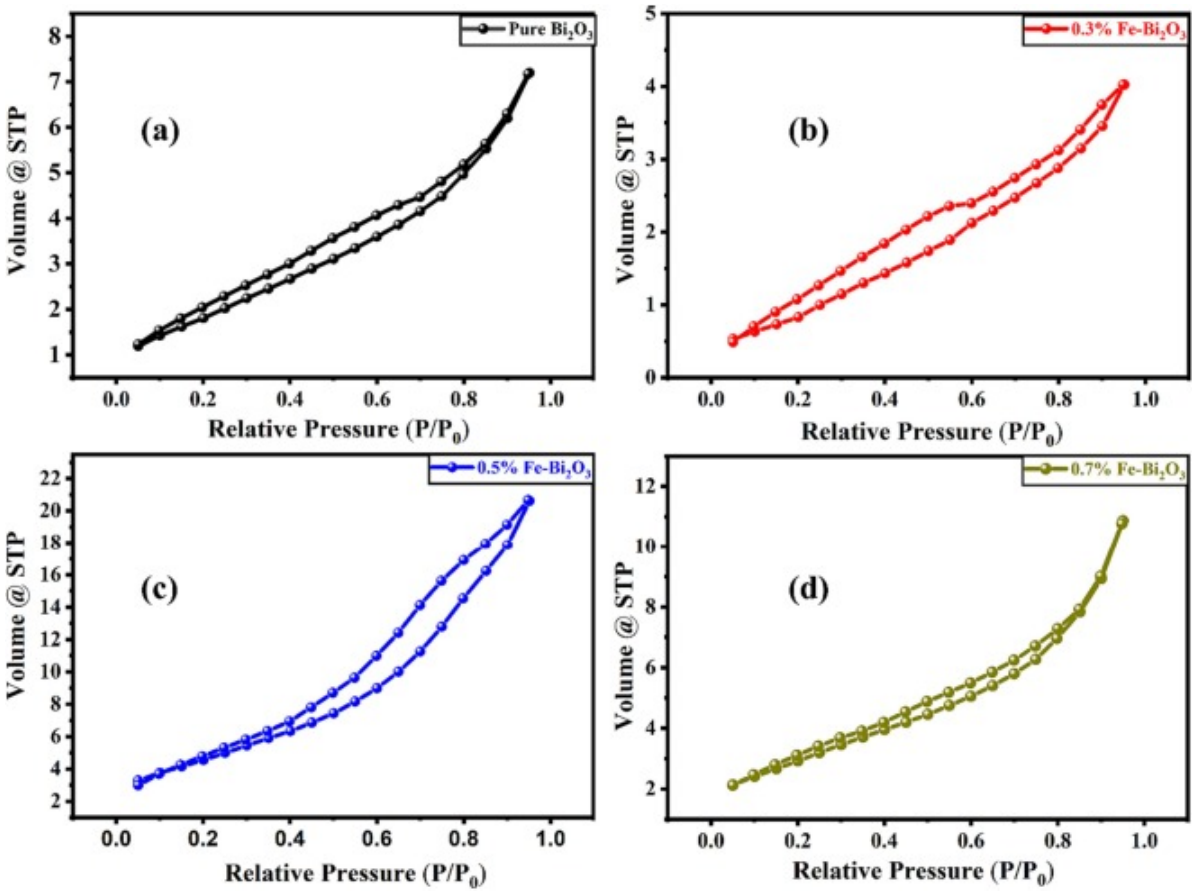

Download : Download high-res image (332KB)

Download : Download full-size image

Fig. 11. N_2adsorption–desorption isotherms of the pure and Fe-doped Bi_2O_3 nanorods with concentrations 0, 0.3, 0.5, and 0.7%.

Photoluminescence studies

Analysis of the photoluminescence spectrum is an effective method for examining the semiconductor's ability to separate the electron-hole pair produced by a photon. The optical absorption spectra of Bi_2O_3 nanoparticles are seen in Fig. 12. The optical transmission of the initial excitation state is responsible for the maxima at 450 nm. Therefore, we may say that the pure synthesized sample of Bi_2O_3 has an excitation band at 450 nm. The quantum-confinement effect of the Bi_2O_3 nanoparticles may be responsible for the clear blue shift of the absorption peak in comparison to bulk bismuth. In the visible range, there was a broad green emission band at 527–563 nm that was caused by several intrinsic or extrinsic defects as well as surface or oxygen vacancy defects [3]. The peak shifts to a shorter wavelength of 428 nm after doping. Therefore, the excitation peak for the Fe-doped Bi_2O_3 is at 428 nm. To stop the rapid recombination of photogenerated charge carriers, Fe ions might be utilized as an electron acceptor that can be activated by light [62]. It is possible to identify the visible emission as the result of the radiative recombination of an electron occupying the oxygen and bismuth vacancies with a photogenerated hole. The electronic transition

may cause the blue-green emission peak to arise at 486 nm. Due to the recombination of photogenerated holes and electrons trapped by singly ionised oxygen vacancies, the green emission peak cantered about 537 nm is attributed to defects related to oxygen vacancies [63]. The 0.5% Fe-doped Bi_2O_3 nanorod exhibits a greater fluorescence intensity than all other samples, as shown in the blue and green emission spectra. An increase in the intensity of the green emission may indicate that there are more defects in the 0.5% Fe-doped Bi_2O_3 nanorods, which may be crucial to the photocatalytic activity. The effectiveness of interfacial transmission of charges to adsorbed materials is improved by efficient charge separation, which also prolongs the life of charge carriers and enhances photocatalytic activity [16].

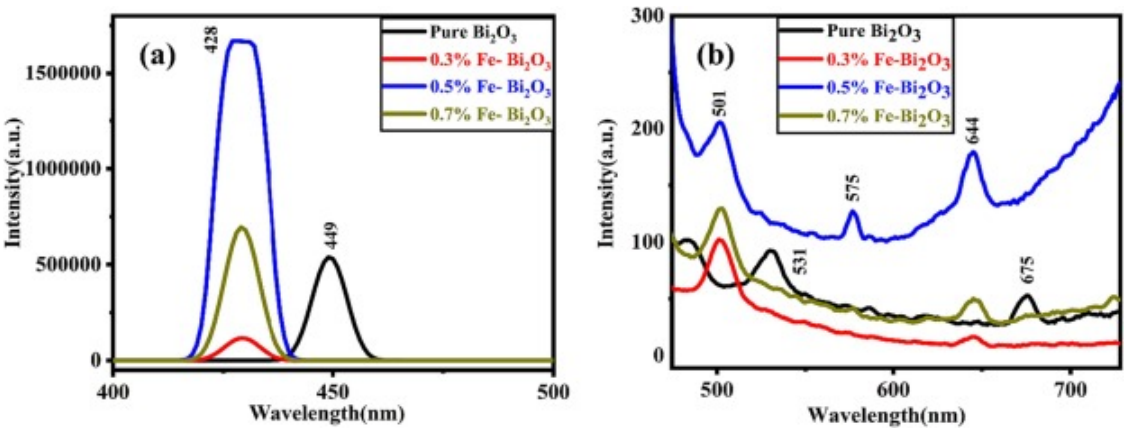

Download : Download high-res image (223KB)

Download : Download full-size image

Fig. 12. PL spectra of of Pure Bi_2O_3 and 0.3%, 0.5% and 0.7% Fe doped Bi_2O_3.

Antibacterial application

Using the good diffusion method and dark conditions, the bactericidal activity of pure Bi_2O_3 and Fe-doped Bi_2O_3 at different concentrations (0.3%, 0.5%, and 0.7%) was examined. In Table 9, the zone of inhibition of synthesized material against Bacillus is shown. According to the zone of inhibition method's findings, both pure and Fe-doped Bi_2O_3 exhibit noticeable inhibition surrounding material (Fig. 13). For pure and (0.3, 0.5, 0.7%) Fe-doped Bi_2O_3, the inhibitory zones were 17 mm, 18 mm, 20 mm, and 19 mm. Comparing the 0.5% Fe-doped nanostructure to other Fe-doped nanostructures, it was discovered that it had greater antibacterial activity against the Gram-negative bacteria Bacillus.

Table 9. Values of surface area pore volume and pore radius of pure and Fe doped Bi_2O_3.

Sample	Surface area (m2/g)	Pore Volume (cc/g)	Pore Radius
Pure Bi_2O_3	7.722	0.01212	0.3138
0.3% Fe-Bi_2O_3	3.765	0.00520	0.3589

Sample	Surface area (m2/g)	Pore Volume (cc/g)	Pore Radius
0.5% Fe-Bi_2O_3	21.732	0.02860	0.2631
0.7% Fe-Bi_2O_3	11.704	0.01776	0.3035

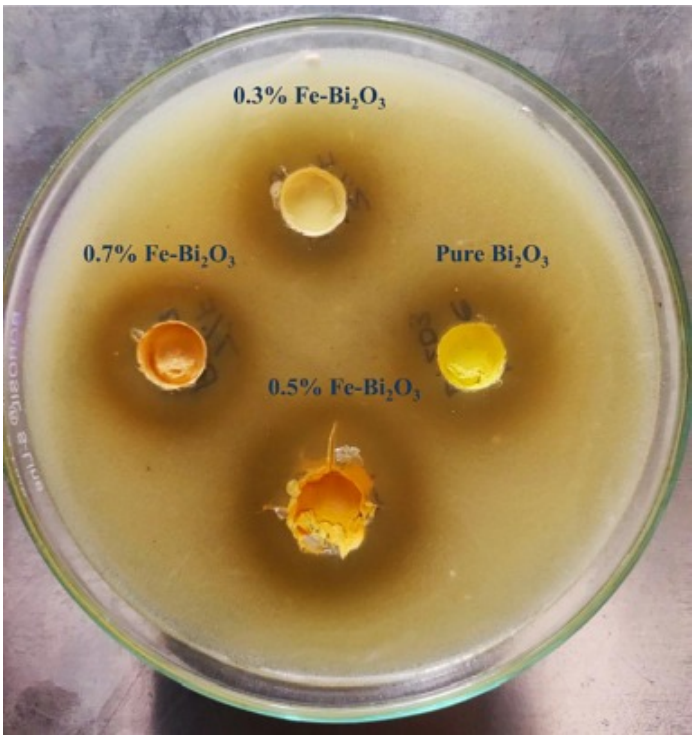

Download : Download high-res image (134KB)

Download : Download full-size image

Fig. 13. Antibacterial activity of Pure Bi_2O_3 and (0.3%, 0.5%, and 0.7%) Fe-doped Bi_2O_3 for different concentrations.

The results reveal that the antibacterial activity of pure and Fe-doped Bi_2O_3 nanostructures increases in the following order: 0.5 wt% Fe-doped Bi_2O_3 > 0.7% Fe-doped Bi_2O_3 > 0.3 wt% Fe-doped Bi_2O_3 > pure Bi_2O_3. Much literature reported the relationship between the outer membrane and cell wall of bacteria being destroyed by reactive oxygen species such as O_2 and OH and H_2O_2. As the synthesized material shows super magnetic behavior so it shows greater antibacterial The increase in oxygen vacancies in the Fe-doped Bi_2O_3 nanomaterials may explain the improvement in antibacterial activity resulting from Fe doping. When compared to pure Bi_2O_3 nanostructures, it makes the particles positively charged and thus increases the electrostatic attraction between the particles that are positively charged and the negative cell wall surface with a higher number of reactive oxygen species (ROS), promoting the efficiency of the antibacterial effect against bacteria [57]. The effect of Fe-doped Bi_2O_3 nanorod's high antibacterial activity can be assigned to their chemical composition, tendency for metal ion release, and magnetization improvement, which

results in the transmembrane transfer of electrons increase in surface area, providing more active sites, penetration, and oxidation of cell components, generation of reactive oxygen species during, promoting bacterial cell damage. This oxidative stress, coupled with increased surface interactions, leads to improved antibacterial efficacy [64].

Antifungal application

The antifungal activity of pure Bi_2O_3 and (0.3, 0.5, 0.7%) Fe-doped Bi_2O_3 at various doses against Aspergillus flavus fungal cultures were examined and depicted in Fig. 14. The diameter of the growth inhibition zone (mm) was measured and included in Table 10. Increased Fe concentrations promote antifungal activity, similar to the effects of antibacterial activities. The diameter of zone inhibition for pure Bi_2O_3 and(0.3, 0.5, 0.7%) Fe doped Bi_2O_3 is given as 15, 16, 23, and 20mm. The Fe-doped Bi_2O_3 samples were more effective against fungus than the pure Bi_2O_3. As pure and Fe-doped Bi_2O_3 show superparamagnetic gesture but 0.5% Fe-doped Bi_2O_3 shows maximum magnetization which enhances the antifungal activity of the sample. The 0.5% Fe-doped Bi_2O_3 with the maximal inhibition zone had the greatest antifungal efficiency against Fungi. It might be because of the 0.5% Fe doped Bi_2O_3 sample's unusually small crystallite size or high accessible surface area, which increases contact and friction and allows the sample to enter the cell through the pores of plasma membrane proteins, causing cell death [65]. See Table 11..

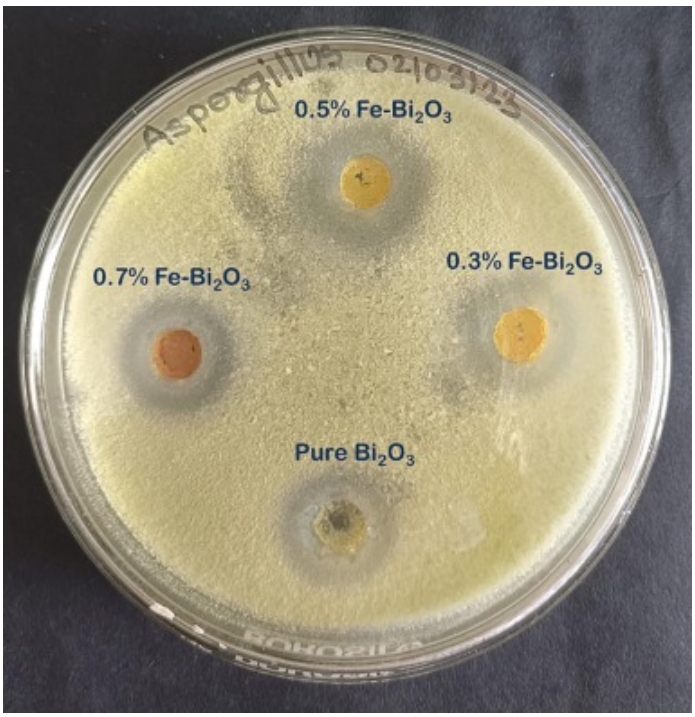

Download : Download high-res image (242KB)

Download : Download full-size image

Fig. 14. Antifungal activity of Pure Bi_2O_3 and Fe-doped Bi_2O_3 for different concentrations (0.3%, 0.5%, and 0.7%).

Table 10. The diameter of zone inhibition of Pure and Fe-doped Bi_2O_3.

Samples	Diameter of Zone Inhibition (mm)
Pure Bi_2O_3	17
0.3% Fe- Bi_2O_3	18
0.5% Fe- Bi_2O_3	20
0.7% Fe- Bi_2O_3	19

Table 11. The diameter of zone inhibition of Pure and Fe-doped Bi_2O_3.

Samples	Diameter of Zone Inhibition (mm)
Pure Bi_2O_3	15
0.3% Fe- Bi_2O_3	18
0.5% Fe- Bi_2O_3	23
0.7% Fe- Bi_2O_3	20

Conclusion

In this present work pure and Fe-doped Bi_2O_3 nanorods were synthesized using hydrothermal method. Fe doping induced phase change, variations in crystalline size, surface area, magnetization, decreased band gap, and defect formations. The 0.5% Fe-doped Bi_2O_3 sample exhibited the highest specific surface area (21.732 m2/g), resulting in remarkable photocatalytic efficiency (93.37%). It displayed strong antimicrobial properties, with significant inhibitory zones (20 mm for bacteria, 23 mm for fungi) attributed to smaller size, increased surface area, defects, and enhanced magnetization. This research underscores Fe doping's role in tailoring Bi_2O_3 nanorods for advanced photocatalysis and antimicrobial applications.

Declaration of Competing Interest

The authors declare that they have no known competing financial interests or personal relationships that could have appeared to influence the work reported in this paper.

Acknowledgment

The author V. A. Mane gratefully acknowledges the generous support of the Chhatrapati Shahu Maharaj Research, Training and Human Development Institute (SARTHI), Pune for financial assistance through fellowship Ref No. CSMNRF-2022/2022-23/2341, India.

Special issue articles Recommended articles

Data availability

The data that has been used is confidential.

References

[1] D.V. Dake, N.D. Raskar, V.A. Mane, R.B. Sonpir, E. Stathatos, K. Asokan, P.D. Babu, B.N. Dole
Exploring the role of defects on diverse properties of Cr-substituted ZnS nanostructures for photocatalytic applications
Appl. Phys. A, 126 (8) (2020), p. 640
View in Scopus Google Scholar

[2] J. Schneider, M. Matsuoka, M. Takeuchi, J. Zhang, Y. Horiuchi, M. Anpo, D.W. Bahnemann
Understanding TiO2 photocatalysis: mechanisms and materials
Chem. Rev., 114 (19) (2014), pp. 9919-9986
CrossRef View in Scopus Google Scholar

[3] N.D. Raskar, D.V. Dake, V.A. Mane, E. Stathatos, U. Deshpande, B. Dole
One step synthesis of vertically grown Mn-doped ZnO nanorods for photocatalytic application
J. Mater. Sci. Mater. Electron., 30 (11) (2019), pp. 10886-10899
CrossRef View in Scopus Google Scholar

[4] D.V. Dake, R.B. Sonpir, V.A. Mane, N.D. Raskar, H.A. Khawal, U. Deshpande, B.N. Dole
Inferring the physical properties of La-substituted ZnO nanorods and nanoflowers for the photodegradation of Congo red azo dye
J. Mater. Sci. Mater. Electron., 33 (11) (2022), pp. 8880-8892
CrossRef View in Scopus Google Scholar

[5] O. Koysuren, H.N. Koysuren
Application of CuO and its composite with polyaniline on the photocatalytic degradation of methylene blue and the Cr(VI) photoreduction under visible light
J. Sol-Gel Sci. Technol., 106 (1) (2023), pp. 131-148
CrossRef View in Scopus Google Scholar

[6] K.P. Gattu, A.A. Kashale, K. Ghule, V.H. Ingole, R. Sharma, N.G. Deshpande, A.V. Ghule
NO2 sensing studies of bio-green synthesized Au-doped SnO2
J. Mater. Sci. Mater. Electron., 28 (17) (2017), pp. 13209-13216

CrossRef ↗ View in Scopus ↗ Google Scholar ↗

[7] R.P. Dighole, A.V. Munde, B.B. Mulik, B.R. Sathe
Bi2O3 nanoparticles decorated carbon nanotube: an effective nanoelectrode for enhanced electrocatalytic 4-nitrophenol reduction
Front. Chem., 8 (2020)
Google Scholar ↗

[8] E. Hashemi, R. Poursalehi, H. Delavari
Formation mechanisms, structural and optical properties of Bi/Bi2O3 One dimensional nanostructures prepared via oriented aggregation of bismuth based nanoparticles synthesized by DC arc discharge in water
Mater. Sci. Semicond. Process., 89 (2019), pp. 51-58
View PDF View article View in Scopus ↗ Google Scholar ↗

[9] A. Rufus, N. Sreeju, D. Philip
Synthesis of biogenic hematite (α-Fe2O3) nanoparticles for antibacterial and nanofluid applications
RSC Adv., 6 (96) (2016), pp. 94206-94217
View in Scopus ↗ Google Scholar ↗

[10] T. Munawar, M.S. Nadeem, F. Mukhtar, M.N.U. Rehman, M. Riaz, S. Batool, M. Hasan, F. Iqbal
Transition metal-doped SnO(2) and graphene oxide
Environ. Sci. Pollut. Res., 29 (60) (2022), pp. 90995-91016
CrossRef ↗ View in Scopus ↗ Google Scholar ↗

[11] A.A. Qureshi, S. Javed, H.M.A. Javed, A. Akram, M.S. Mustafa, U. Ali, M.Z. Nisar
Facile formation of SnO2–TiO2 based photoanode and Fe3O4@rGO based counter electrode for efficient dye-sensitized solar cells
Mater. Sci. Semicond. Process., 123 (2021), Article 105545
View PDF View article View in Scopus ↗ Google Scholar ↗

[12] S. Ramachandran, A. Sivasamy
Synthesis of nanocrystalline bismuth oxide and its visible photocatalytic activity in the degradation of an organic dye
Inorganic and Nano-Metal Chemistry, 48 (4–5) (2018), pp. 225-232
CrossRef ↗ View in Scopus ↗ Google Scholar ↗

[13] X. Hu, Y. Zhang, T. Ding, J. Liu, H. Zhao
Multifunctional gold nanoparticles: a novel nanomaterial for various medical applications and biological activities

Front. Bioeng. Biotechnol., 8 (2020)

Google Scholar ↗

[14] B. Calderón-Jiménez, M. Johnson, A. Montoro Bustos, K. Murphy, M. Winchester, J. Vega-Baudrit

Silver nanoparticles: technological advances, societal impacts, and metrological challenges

Frontiers Chemistry, 5 (2017)

Google Scholar ↗

[15] A. Dere, M. Soylu, F. Yakuphanoglu

Solar light sensitive photodiode produced using a coumarin doped bismuth oxide composite

Mater. Sci. Semicond. Process., 90 (2019), pp. 129-142

View PDF View article View in Scopus ↗ Google Scholar ↗

[16] G. Viruthagiri, P. Kannan, V. Indhumathi, Photocatalytic activity of α-Phase bismuth oxide nanoparticles under visible light, 2 (2017) 2455-4227.

Google Scholar ↗

[17] C.H. Ho, C.H. Chan, Y.S. Huang, L.C. Tien, L.C. Chao

The study of optical band edge property of bismuth oxide nanowires α-Bi2O3

Opt. Express, 21 (10) (2013), pp. 11965-11972

View in Scopus ↗ Google Scholar ↗

[18] H.-Y. Jiang, P. Li, G. liu, J. Ye, J. Lin

Synthesis and photocatalytic properties of metastable β-Bi2O3 stabilized by surface-coordination effects

J. Mater. Chem. A, 3 (9) (2015), pp. 5119-5125

View in Scopus ↗ Google Scholar ↗

[19] J. Wu, F. Wang, H. Li, S. Yang, P. Li, Y. Zhao, Y. Li, T. Zhai

Epitaxial growth of 2D ultrathin metastable γ-Bi2O3 flakes for high performance ultraviolet photodetection

Small, 18 (3) (2022), p. 2104244

View in Scopus ↗ Google Scholar ↗

[20] H. Sudrajat, P. Sujaridworakun

Low-temperature synthesis of δ-Bi2O3 hierarchical nanostructures composed of ultrathin nanosheets for efficient photocatalysis

Mater. Des., 130 (2017), pp. 501-511

View PDF View article View in Scopus ↗ Google Scholar ↗

[21] N. Kumada, N. Kinomura
A New Allotropic Form of Bi2O3
MRS Proc., 547 (1998), p. 227
Google Scholar

[22] Z. Xu, C. Han, J. Xie
Synthesis of ω-Bi2O3 micropyramids with excellent photocatalytic properties
Micro & Nano Letters, 15 (4) (2020), pp. 218-220
CrossRef View in Scopus Google Scholar

[23] A.H. Zahid, Q. Han
A review on the preparation, microstructure, and photocatalytic performance of Bi2O3 in polymorphs
Nanoscale, 13 (42) (2021), pp. 17687-17724
CrossRef View in Scopus Google Scholar

[24] M. Ahamed, M.J. Akhtar, M.A.M. Khan, Z.M. Alaizeri, H. Alhadlaq
Facile synthesis of Zn-Doped Bi2O3 nanoparticles and their selective cytotoxicity toward cancer cells
ACS Omega, 6 (27) (2021), pp. 17353-17361
CrossRef View in Scopus Google Scholar

[25] L. Wang, C. Hu, L. Shao
The antimicrobial activity of nanoparticles: present situation and prospects for the future
Int. J. Nanomed., 12 (2017), pp. 1227-1249
View in Scopus Google Scholar

[26] J. Liang, G. Zhu, P. Liu, X. Luo, C. Tan, L. Jin, J. Zhou
Synthesis and characterization of Fe-doped β-Bi2O3 porous microspheres with enhanced visible light photocatalytic activity
Superlattice. Microst., 72 (2014), pp. 272-282
View PDF View article View in Scopus Google Scholar

[27] G.K. Dinesh, S. Anandan, T. Sivasankar
Synthesis of Fe-doped Bi(2)O(3) nanocatalyst and its sonophotocatalytic activity on synthetic dye and real textile wastewater
Environ. Sci. Pollut. Res. Int., 23 (20) (2016), pp. 20100-20110
CrossRef View in Scopus Google Scholar

[28] M.-H. Vu, C.-C. Nguyen, T.-O. Do

Synergistic effect of Fe doping and plasmonic Au nanoparticles on W18O49 nanorods for enhancing photoelectrochemical nitrogen reduction

ACS Sustain. Chem. Eng., 8 (32) (2020), pp. 12321-12330

CrossRef ↗ View in Scopus ↗ Google Scholar ↗

[29] A.Z. Alshemary, A. Engin Pazarceviren, A. Tezcaner, Z. Evis

Fe3+/− dual doped nano hydroxyapatite: a novel material for biomedical applications

Journal of Biomedical Materials Research Part B: Applied Biomaterials, 106 (1) (2018), pp. 340-352

CrossRef ↗ View in Scopus ↗ Google Scholar ↗

[30] S. Sood, A. Umar, S. Kumar Mehta, S. Kumar Kansal

α-Bi2O3 nanorods: An efficient sunlight active photocatalyst for degradation of Rhodamine B and 2,4,6-trichlorophenol

Ceram. Int., 41 (3, Part A) (2015), pp. 3355-3364

View PDF View article View in Scopus ↗ Google Scholar ↗

[31] S.E. Musavi Ghahfarokhi, M.R. Larki, I. Kazeminezhad

The effect of Mn doped on the structural, magnetic, dielectric and optical properties of bismuth ferrite (BiFe1-xMnxO3) nanoparticles

Vacuum, 173 (2020), Article 109143

View PDF View article View in Scopus ↗ Google Scholar ↗

[32] V. Fruth, M. Popa, D. Berger, C.M. Ionica, M. Jitianu

Phases investigation in the antimony doped Bi2O3 system

J. Eur. Ceram. Soc., 24 (6) (2004), pp. 1295-1299

View PDF View article View in Scopus ↗ Google Scholar ↗

[33] B.A. Utami, H. Sutanto, I. Alkian, F. Sa'Adah, E. Hidayanto

Efficient degradation of amoxicillin using Bi 2 O 3/Fe synthesized by microwave-assisted precipitation method

Cogent Engineering, 9 (1) (2022)

Google Scholar ↗

[34] J. Oh, H. Ryu, W.-J. Lee

Effects of Fe doping on the photoelectrochemical properties of CuO photoelectrodes

Compos. B Eng., 163 (2019), pp. 59-66

View PDF View article CrossRef ↗ View in Scopus ↗ Google Scholar ↗

[35] S.V. Kite, A.N. Kadam, D.J. Sathe, S. Patil, S.S. Mali, C.K. Hong, S.W. Lee, K.M. Garadkar

Nanostructured TiO(2) sensitized with MoS(2) nanoflowers for enhanced photodegradation efficiency toward methyl orange

ACS Omega, 6 (26) (2021), pp. 17071-17085

CrossRef ↗ View in Scopus ↗ Google Scholar ↗

[36] Y. Astuti, R. Andianingrum, A. Arnelli, A.D. Haris

The role of H2C2O4 and Na2CO3 as precipitating agents on the physichochemical properties and photocatalytic activity of bismuth oxide

Open Chemistry, 18 (2020), pp. 129-137

CrossRef ↗ View in Scopus ↗ Google Scholar ↗

[37] L. Baia, R. Stefan, W. Kiefer, S. Simon

Structural characteristics of B2O3Bi2O3 glasses with high transition metal oxide content

J. Raman Spectrosc., 36 (3) (2005), pp. 262-266

CrossRef ↗ View in Scopus ↗ Google Scholar ↗

[38] S. Labib

Preparation, characterization and photocatalytic properties of doped and undoped Bi2O3

J. Saudi Chem. Soc., 21 (6) (2017), pp. 664-672

View PDF View article View in Scopus ↗ Google Scholar ↗

[39] I. Bibi, S. Iqbal, F. Majid, S. Kamal, Q. Raza, M. Amami, K.M. Katubi, N. Alwadai, M. Asad Kareem, M. Iqbal

The effect of Zn and Ni doping on the structural, optical, dielectric and photocatalytic properties of Sr1-xZnxFe1-yNiyO19

Results Phys., 40 (2022), Article 105868

View PDF View article View in Scopus ↗ Google Scholar ↗

[40] S.B. Somvanshi, M.V. Khedkar, P.B. Kharat, K.M. Jadhav

Influential diamagnetic magnesium (Mg2+) ion substitution in nano-spinel zinc ferrite (ZnFe2O4): Thermal, structural, spectral, optical and physisorption analysis

Ceram. Int., 46 (7) (2020), pp. 8640-8650

View PDF View article View in Scopus ↗ Google Scholar ↗

[41] D.V. Dake, N.D. Raskar, V.A. Mane, R.B. Sonpir, H.A. Khawal, U. Deshpande, E. Stathatos, B.N. Dole

Photocatalytic performance of graphene-based Cr-substituted β ZnS nanocomposites

Appl. Phys. A, 128 (4) (2022), p. 276

View in Scopus ↗ Google Scholar ↗

[42] N. Prasad, K. Balasubramanian
Raman spectral probe on increased local vibrational modes and phonon lifetimes in Ho3+-doped Bi2O3 micro-rods
J. Raman Spectrosc., 47 (10) (2016), pp. 1266-1270
CrossRef ↗ View in Scopus ↗ Google Scholar ↗

[43] J.J. Beltran, L.C. Sánchez, J. Osorio, L. Tirado, E.M. Baggio-Saitovitch, C.A. Barrero
Crystallographic and magnetic properties of Fe-doped SnO2 nanopowders obtained by a sol–gel method
J. Mater. Sci., 45 (18) (2010), pp. 5002-5011
CrossRef ↗ View in Scopus ↗ Google Scholar ↗

[44] B. Karthikeyan, D.R. Udayabhaskar, M.R. Ashwin Kishore
Optical and phonon properties of Sm-doped a-Bi 2 O 3 micro rods
Appl. Phys. A, 117 (2014), pp. 1409-1414
CrossRef ↗ View in Scopus ↗ Google Scholar ↗

[45] A.J. Salazar-Pérez, M. Camacho-Lopez, R.A. Morales Luckie, V. Sanchez-Mendieta, F. Ureña-Nuñez, J. Arenas-Alatorre
Structural evolution of Bi2O3 prepared by thermal oxidation of bismuth nano-particles
Superficies y Vacío, 18 (2005), pp. 4-8
Google Scholar ↗

[46] L. Kumari, J.-H. Lin, Y.-R. Ma
Laser oxidation and wide-band photoluminescence of thermal evaporated bismuth thin films
J. Phys. D Appl. Phys., 41 (2) (2008), Article 025405
CrossRef ↗ View in Scopus ↗ Google Scholar ↗

[47] P. Liu, Z. Cheng, Y. Du, X.-L. Wang
Effects of Cu and Fe doping on Raman spectra and on the structural and magnetic properties of ErMnO3
J. Appl. Phys., 109 (2011), p. 07D710
View in Scopus ↗ Google Scholar ↗

[48] S. Bandyopadhyay, A. Dutta
Microstructural interpretation of vibrational properties and ionic transport mechanism in Dy stabilized δ-Bi2O3
J. Alloy. Compd., 682 (2016), pp. 80-88
View PDF View article View in Scopus ↗ Google Scholar ↗

[49] O. Depablos-Rivera, A. Martínez, S.E. Rodil
Interpretation of the Raman spectra of bismuth oxide thin films presenting different crystallographic phases
J. Alloy. Compd., 853 (2021), Article 157245
View PDF View article View in Scopus ↗ Google Scholar ↗

[50] K. Badreddine, A. Srour, R. Awad, A.I. Abou-Aly
The investigation of mechanical and dielectric properties of samarium doped ZnO nanoparticles
Mater. Res. Express, 7 (2) (2020), p. 025016
CrossRef ↗ View in Scopus ↗ Google Scholar ↗

[51] G.K. Dinesh, S. Anandan, T. Sivasankar
Synthesis of Fe-doped Bi2O3 nanocatalyst and its sonophotocatalytic activity on synthetic dye and real textile wastewater
Environ. Sci. Pollut. Res., 23 (20) (2016), pp. 20100-20110
CrossRef ↗ View in Scopus ↗ Google Scholar ↗

[52] B. Mallesham, S. Roy, S. Bose, A.N. Nair, S. Sreenivasan, V. Shutthanandan, C.V. Ramana
Crystal chemistry, band-gap red shift, and electrocatalytic activity of iron-doped gallium oxide ceramics
ACS Omega, 5 (1) (2020), pp. 104-112
CrossRef ↗ View in Scopus ↗ Google Scholar ↗

[53] Y. Ying, F. Tao, T. Hong, L. Wang
Controlled fabrication of bismuth vanadium oxide hierarchical microtubes with enhanced visible light photocatalytic activity
Mater. Sci. Semicond. Process., 32 (2015), pp. 82-89
View PDF View article View in Scopus ↗ Google Scholar ↗

[54] M. Mersal, A. Zedan, G. Mohamed, G. Hassan
Fabrication of nitrogen doped TiO2/Fe2O3 nanostructures for photocatalytic oxidation of methanol based wastewater
Sci. Rep., 13 (2023)
Google Scholar ↗

[55] S.P. John, J.M. Mathew
Determination of ferrimagnetic and superparamagnetic components of magnetization and the effect of particle size on structural, magnetic and hyperfine properties of Mg0.5Zn0.5Fe2O4 nanoparticles
J. Alloy. Compd., 869 (2021), Article 159242

View PDF View article View in Scopus ↗ Google Scholar ↗

[56] S.B. Somvanshi, S.R. Patade, D.D. Andhare, S.A. Jadhav, M.V. Khedkar, P.B. Kharat, P.P. Khirade, K.M. Jadhav

Hyperthermic evaluation of oleic acid coated nano-spinel magnesium ferrite: Enhancement via hydrophobic-to-hydrophilic surface transformation

J. Alloy. Compd., 835 (2020), Article 155422

View PDF View article View in Scopus ↗ Google Scholar ↗

[57] N.M. Basith, J.J. Vijaya, L.J. Kennedy, M. Bououdina, R. Shenbhagaraman, R. Jayavel

Influence of Fe-doping on the structural, morphological, optical, magnetic and antibacterial effect of ZnO nanostructures

J. Nanosci. Nanotechnol., 16 (2) (2016), pp. 1567-1577

View in Scopus ↗ Google Scholar ↗

[58] O. Koysuren, H.N. Koysuren

Photocatalytic activity of polyaniline/Fe-doped TiO2 composites by in situ polymerization method

J. Macromol. Sci. A, 56 (3) (2019), pp. 267-276

CrossRef ↗ View in Scopus ↗ Google Scholar ↗

[59] R. Saleh, N.F. Djaja

UV light photocatalytic degradation of organic dyes with Fe-doped ZnO nanoparticles

Superlattice. Microst., 74 (2014), pp. 217-233

View PDF View article View in Scopus ↗ Google Scholar ↗

[60] M.L. Matias, A. Pimentel, A.S. Reis-Machado, J. Rodrigues, J. Deuermeier, E. Fortunato, R. Martins, D. Nunes, Enhanced Fe-TiO(2) Solar Photocatalysts on Porous Platforms for Water Purification, Nanomaterials (Basel) 12(6) (2022).

Google Scholar ↗

[61] I. Shahzadi, M. Aqeel, A. Haider, S. Naz, M. Imran, W. Nabgan, A. Al-Shanini, A. Shahzadi, T. Alshahrani, M. Ikram

Hydrothermal synthesis of fe-doped cadmium oxide showed bactericidal behavior and highly efficient visible light photocatalysis

ACS Omega, 8 (33) (2023), pp. 30681-30693

CrossRef ↗ View in Scopus ↗ Google Scholar ↗

[62] Y. Zhu, J. Xue, T. Xu, G. He, H. Chen

Enhanced photocatalytic activity of magnetic core–shell Fe3O4@Bi2O3–RGO

heterojunctions for quinolone antibiotics degradation under visible light

J. Mater. Sci. Mater. Electron., 28 (2017), pp. 1-10

View PDF View article Google Scholar

[63] B. Maibam, S. Baruah, S. Kumar

Photoluminescence and intrinsic ferromagnetism of Fe doped zinc oxide

SN Applied Sciences, 2 (10) (2020), p. 1712

View in Scopus Google Scholar

[64] M.A. Faraj, M.A. Jabbar, A.N. Abd, Inhibitory Effect of Bi2O3NPs Produced by green synthesis method, Journal of Physics: Conference Series 2322(1) (2022) 012083.

Google Scholar

[65] M. Shahzad Shirazi, M. Moridi Farimani, A. Foroumadi, K. Ghanemi, M. Benaglia, P. Makvandi

Bioengineered synthesis of phytochemical-adorned green silver oxide (Ag2O) nanoparticles via Mentha pulegium and Ficus carica extracts with high antioxidant, antibacterial, and antifungal activities

Sci. Rep., 12 (1) (2022), Article 21509

View in Scopus Google Scholar

Cited by (8)

A review on Bi<inf>2</inf>O<inf>3</inf> nanomaterial for photocatalytic and antibacterial applications

2024, Chemical Physics Impact

Show abstract

Growth in defects and surface area for the photocatalytic performance of GO-based Fe-doped bismuth oxide mesoporous nanocomposite

2024, Ceramics International

Show abstract

Magneto-chemical properties of Ti-doped Co<inf>3</inf>O<inf>4</inf> nanosheets for photocatalytic activity applications

2024, Materials Today Communications

Show abstract

Experimental evaluation of gamma radiation attenuation properties of Ni<inf>0.2</inf>Mg<inf>x</inf>Zn<inf>0.8-x</inf>Fe<inf>2</inf>O<inf>4</inf>

2024, Optical Materials

Show abstract

Photocatalytic efficiency of GO-based Ti-doped Co<inf>3</inf>O<inf>4</inf> nanosheets for mixed dyes and the effects of oxidizing and reducing reagents

2024, Ceramics International

Show abstract

Enhanced Performance of Fe/WO<inf>3</inf> Terahertz Dielectric Lenses

2024, Crystal Research and Technology

View all citing articles on Scopus